

# Estimating the Integrated Bispectrum from Weak Lensing Maps

D. Munshi<sup>a</sup>, J. D. McEwen<sup>b</sup>, T. Kitching<sup>c</sup>  
P. Fosalba<sup>d,e</sup>, R. Teyssier<sup>f</sup>, J. Stadel<sup>g</sup>

<sup>a,b,c</sup> Mullard Space Science Laboratory,  
University College London, Holmbury St Mary,  
Dorking, Surrey RH5 6NT, UK

<sup>d</sup> Institute of Space Sciences (ICE, CSIC), Campus UAB,  
Carrer de Can Magrans, s/n, 08193 Barcelona, Spain

<sup>e</sup> Institut d'Estudis Espacials de Catalunya (IEEC),  
E-08034 Barcelona, Spain

<sup>f,g</sup> Institute for Computational Science, University of Zurich,  
Winterthurerstrasse 190, 8057 Zurich, Switzerland

E-mail: <sup>a</sup>[D.Munshi@ucl.ac.uk](mailto:D.Munshi@ucl.ac.uk), <sup>b</sup>[Jason.McEwen@ucl.ac.uk](mailto:Jason.McEwen@ucl.ac.uk), <sup>c</sup>[t.kitching@ucl.ac.uk](mailto:t.kitching@ucl.ac.uk),  
<sup>d</sup>[fosalba@ieec.uab.es](mailto:fosalba@ieec.uab.es), <sup>f</sup>[romain.teyssier@uzh.ch](mailto:romain.teyssier@uzh.ch), <sup>g</sup>[stadel@physik.uzh.ch](mailto:stadel@physik.uzh.ch)

**Abstract.** We use a recently introduced statistic called *Integrated Bispectrum* (IB) to probe the gravity-induced non-Gaussianity at the level of the bispectrum from weak lensing convergence or  $\kappa$  maps. We generalize the concept of the IB to spherical coordinates, This result is next connected to the response function approach. We introduce the concept of squeezed three point correlation functions (3PCF) for  $\kappa$  maps and relate them to the IB defined in the Fourier domain. Finally, we use the Euclid Flagship simulations to compute the IB as a function of redshift and wave number. We outline how IB can be computed using a variety of analytical approaches including ones based on *Effective Field Theory* (EFT), *Halo models* and models based on the *Separate Universe approach*. Generalizations to include tomographic bins, external data sets and Bayesian estimators are discussed. Generalizations to shear maps and construction of squeezed limits of EEE, BBB, EEB and EEB bispectra are also discussed. We also show how external data sets, e.g.  $y$ -parameter maps from thermal Sunyaev-Zeldovich observations, can be used to construct the squeezed limits of mixed IB involving  $y$  and  $\kappa$  fields. We emphasize the role of the finite volume effect in numerical estimation of IB.

**Keywords:** Cosmology, Large-Scale Structure, Weak Lensing

---

## Contents

<b>1</b>	<b>Introduction</b>	<b>1</b>
<b>2</b>	<b>Position-Dependent Power Spectrum from Convergence Maps</b>	<b>2</b>
2.1	Flat-Sky Treatment	3
2.2	Zeldovich Approximation	6
2.3	Response Function Approach	7
2.4	All-Sky Formulation	7
<b>3</b>	<b>Analytical Modelling of IB</b>	<b>9</b>
3.1	Halo Model	9
3.2	Effective Field Theory (EFT)	10
3.3	Linear Response Function and Separate Universe Approach	12
<b>4</b>	<b><i>Euclid</i> Flagship Simulations</b>	<b>13</b>
<b>5</b>	<b>Error Budget for IB</b>	<b>15</b>
5.1	Bias	15
5.2	Scatter	15
<b>6</b>	<b>Results and Discussion</b>	<b>16</b>
<b>7</b>	<b>Conclusions and Future Prospects</b>	<b>19</b>
<b>A</b>	<b>Approximate Line-of-Sight Integration</b>	<b>25</b>

---

## 1 Introduction

Thanks to recently completed Cosmic Microwave Background (CMB) experiments, such as the *Planck* Surveyor<sup>1</sup>[1], we now have a standard model of cosmology. However there are many outstanding questions that remain unclear including, but not limited to, the nature of dark matter (DM) and dark energy (DE); or possible modifications of General Relativity (GR) on cosmological scales [2, 3]. In addition the sum of the neutrino masses [4] remains unknown. Fortunately it is expected that the operational weak lensing surveys including CFHTLS<sup>2</sup>, Dark Energy Survey<sup>3</sup>(DES)[5], Dark Energy Spectroscopic Instrument (DESI)<sup>4</sup>, Prime Focus Spectrograph<sup>5</sup>, KiDS[6] and near-future Stage-IV large scale structure (LSS) surveys such as *Euclid*<sup>6</sup>[7], LSST<sup>7</sup>[8] and WFIRST[9] will provide answers to many of the questions that cosmology is facing.

---

<sup>1</sup>Planck

<sup>2</sup><http://www.cfht.hawaii.edu/Sciences/CFHLS>

<sup>3</sup><https://www.darkenergysurvey.org/>

<sup>4</sup><http://desi.lbl.gov>

<sup>5</sup><http://pfs.ipmu.jp>

<sup>6</sup><http://sci.esa.int/euclid/>

<sup>7</sup>[http://www.lsst.org/11st\\_home.shtml](http://www.lsst.org/11st_home.shtml)

Weak lensing, or the minute distortions in the images of the distant galaxies by the intervening large-scale structure allow us to extract information about clustering of the intervening mass distribution in the Universe [10]. The weak lensing surveys are complementary to spectroscopic galaxy redshift surveys such as BOSS<sup>8</sup>[11] or WiggleZ<sup>9</sup>[12] as they provide an unbiased picture of the underlying dark matter distribution, whereas the galaxies and other tracers provide a biased picture [13].

One challenge for weak lensing is that observations are sensitive to smaller scales where clustering is nonlinear and non-Gaussian [14], and therefore difficult to model and measure. A second challenge is that the statistical estimates of cosmological parameters based on power spectrum analyses are typically degenerate in particular cosmological parameter combinations e.g.  $\sigma_8$  and  $\Omega_M$ ; to overcome these degeneracies external data sets (e.g. CMB), and the addition of tomographic or 3D [15] information is typically used. However to address both of these challenges an alternative procedure is to use higher-order statistics that probe the (quasi)nonlinear regime [16–21].

Previously it has been noted that even in the absence of any primordial non-Gaussianity [22], the gravitational clustering induces mode coupling that results in a secondary non-Gaussianity which is more pronounced on smaller scales. Thus a considerable amount of effort has been invested in understanding the gravity induced secondary non-Gaussianity from weak lensing surveys. These statistics include the lower-order cumulants [23] and their correlators [24]; the multispectra including the skew-spectrum [25] and kurtosis spectra [26] as well as the entire PDF [27] and the statistics of hot and cold spots. Future surveys such as *Euclid* will be particularly interesting in this regard. With its large fraction of sky-coverage it will be able to detect the gravity induced non-Gaussianity with a very high signal-to-noise (S/N). It is also worth mentioning here that, in addition to breaking the degeneracy in cosmological parameters, higher-order statistics are also important for a better understanding of the covariance of lower-order estimators [28].

In this paper we will focus on a set of estimators that are particularly sensitive to the squeezed state of the bispectra also known as the *Integrated Bispectra* (IB). These estimators are particularly interesting because of their simplicity, and ease of implementation. While in previous work such estimators have been used in 3D for quantifying galaxy clustering [29] as well as in 1D to probe Lyman- $\alpha$  absorption features [30, 31], our main aim here is to develop these estimators for probing future 2D projected surveys with a focus on weak lensing surveys, and in particular [7].

This paper is organized as follows. In §2 we introduce the position-dependent power spectrum for flat-sky as well as in the all-sky limit. We also present the correspondence between these two cases. The analytical models are discussed in §3. The simulations are presented in §4. An approximate error-analysis is presented in §5. The discussions are presented respectively in §6 and §7. Finally, in Appendix-§A we introduce an approximation that can simplify the evaluation of IB and other projected statistics.

## 2 Position-Dependent Power Spectrum from Convergence Maps

A relatively new observable has been developed in recent years (see e.g. [32]) that relies on the fact that the power spectrum measured from a survey sub-volume correlates with the mean of the same observable in the same sub-volume. This correlation gives a direct estimate

<sup>8</sup><http://www.sdss3.org/surveys/boss.php>

<sup>9</sup><http://wigglez.swin.edu.au/>

of the bispectrum in the *squeezed limit*. Extensions of these results were presented for the divergence of velocity, and in the context of 2D or projected surveys, as well as at higher-order at the level of the squeezed trispectrum [33]. The IB was also derived in redshift-space for a class of modified gravity theories in [36]. In this section we will present the analytical results relevant to the position-dependent power spectrum from 2D surveys with an emphasis particularly on 2D weak lensing surveys.

## 2.1 Flat-Sky Treatment

Measurement of the bispectrum from weak lensing surveys is difficult due to non-ideal sky-coverage caused by masking of regions close to bright objects as well as irregular survey boundaries. The IB proposed here tries to bypass these complexities by concentrating on the squeezed limit of the bispectrum, which can be estimated by techniques developed for estimation of the power spectrum. We will concentrate on the projected survey but generalization to tomographic bins is straight-forward.

In this section we develop the recently introduced statistics of position-dependent power spectrum to the case of weak lensing [33]. We consider 2D weak lensing surveys but extension to 2D projected galaxy surveys can be done in a straight-forward manner. We will use the small angle approximation before generalising to the all-sky case in §2.4.

Let us consider a weak lensing convergence map  $\kappa(\boldsymbol{\theta})$  at a angular position of the sky  $\boldsymbol{\theta}$  defined over a patch of the sky  $\boldsymbol{\theta} = (\vartheta, \varphi)$ , where  $\vartheta$  and  $\varphi$  are R.A. and declination respectively. We will divide the entire patch into equal area sub-patches. We will focus on one such *sub-patch* centered around the angular position  $\boldsymbol{\theta}_0 = (\vartheta_0, \varphi_0)$ . The *local* average of  $\kappa$  on a sub-patch of the sky can differ from its global value of zero, where for a sub-patch the local average is:

$$\bar{\kappa}(\boldsymbol{\theta}_0) := \frac{1}{\alpha} \int d^2\boldsymbol{\theta} \kappa(\boldsymbol{\theta}) W(\boldsymbol{\theta} - \boldsymbol{\theta}_0); \quad \alpha := \int W(\boldsymbol{\theta} - \boldsymbol{\theta}_0) d^2\boldsymbol{\theta}; \quad (2.1a)$$

$$W(\boldsymbol{\theta}) := \Theta(\vartheta - \vartheta_0)\Theta(\varphi - \varphi_0). \quad (2.1b)$$

Here,  $W$  describes the sky-patch and  $\Theta$  represents the unit step function i.e.  $\Theta(\vartheta - \vartheta_0) = 1$  if  $|\vartheta - \vartheta_0| < \vartheta_S$  and zero otherwise and similarly  $\Theta(\varphi - \varphi_0) = 1$  if  $|\varphi - \varphi_0| < \varphi_S$  and zero otherwise. In our notation,  $\vartheta_S$  and  $\varphi_S$  represent half-width of a sub-patch along the  $\vartheta$  and  $\varphi$  directions while  $\alpha$  is the effective area of a sub-patch. We will assume that all sub-patches are of the same size and  $\alpha$  is independent of  $\boldsymbol{\theta}_0$ . In 2D, we will denote the Fourier wave-number as  $\mathbf{l}$  and use the following convention for Fourier Transform:

$$\kappa(\mathbf{l}) := \frac{1}{(2\pi)^2} \int d^2\boldsymbol{\theta} \exp(-i\mathbf{l} \cdot \boldsymbol{\theta}) \kappa(\boldsymbol{\theta}); \quad \kappa(\boldsymbol{\theta}) := \int d^2\mathbf{l} \exp(i\mathbf{l} \cdot \boldsymbol{\theta}) \kappa(\mathbf{l}). \quad (2.2)$$

The power spectrum  $P^\kappa$  and bispectrum  $B^\kappa$  in 2D are defined using the following conventions:

$$\langle \kappa(\mathbf{l}_1) \kappa(\mathbf{l}_2) \rangle := (2\pi)^2 \delta_{2D}(\mathbf{l}_1 + \mathbf{l}_2) P^\kappa(l_1); \quad l = |\mathbf{l}|; \quad (2.3)$$

$$\langle \kappa(\mathbf{l}_1) \kappa(\mathbf{l}_2) \kappa(\mathbf{l}_3) \rangle := (2\pi)^2 \delta_{2D}(\mathbf{l}_1 + \mathbf{l}_2 + \mathbf{l}_3) B^\kappa(\mathbf{l}_1, \mathbf{l}_2, \mathbf{l}_3). \quad (2.4)$$

The angular brackets represent the ensemble average. Here,  $\delta_{2D}$  is the Dirac delta function in 2D. The window  $W$  describing a patch can be used to extend the limits of angular integration. Thus, the flat-sky (local) Fourier transform takes the following form:

$$\kappa(\mathbf{l}; \boldsymbol{\theta}_0) := \int d^2\boldsymbol{\theta} \kappa(\boldsymbol{\theta}) W(\boldsymbol{\theta} - \boldsymbol{\theta}_0) \exp(-i\mathbf{l} \cdot \boldsymbol{\theta}) \quad (2.5a)$$

$$= \int \frac{d^2\mathbf{l}_1}{(2\pi)^2} \kappa(\mathbf{l} - \mathbf{l}_1) W(\mathbf{l}_1) \exp(-i\mathbf{l}_1 \cdot \boldsymbol{\theta}_0). \quad (2.5b)$$

We use  $W(\mathbf{l})$  to denote the Fourier transform of  $W(\boldsymbol{\theta})$ . Notice that the Fourier coefficient  $\kappa(\mathbf{l}; \boldsymbol{\theta}_0)$  for  $\mathbf{l} = 0$  (monopole) is identical to  $\bar{\kappa}(\boldsymbol{\theta}_0)$  defined above. The *local* convergence power spectrum  $P^\kappa(\mathbf{l}; \boldsymbol{\theta}_0)$  in this fraction of sky is given by (we will denote the global power spectrum as  $P^\kappa(\mathbf{l})$ ):

$$P^\kappa(\mathbf{l}; \boldsymbol{\theta}_0) = \frac{1}{\alpha} \int \frac{d^2\mathbf{l}_1}{(2\pi)^2} \int \frac{d^2\mathbf{l}_2}{(2\pi)^2} \kappa(\mathbf{l} - \mathbf{l}_1) \kappa(-\mathbf{l} - \mathbf{l}_2) \times \exp[-i(\mathbf{l}_1 + \mathbf{l}_2) \cdot \boldsymbol{\theta}_0] W(\mathbf{l}_1) W(\mathbf{l}_2). \quad (2.6)$$

The resulting IB is defined by cross-correlating the local estimate of the power spectrum and the local average of the projected field:

$$\begin{aligned} \mathcal{B}^\kappa(\mathbf{l}) &:= \langle P^\kappa(\mathbf{l}; \boldsymbol{\theta}_0) \bar{\kappa}(\boldsymbol{\theta}_0) \rangle; \\ \mathcal{B}^\kappa(\mathbf{l}) &= \frac{1}{\alpha^2} \int \frac{d^2\boldsymbol{\theta}_0}{2\pi} \int \frac{d^2\mathbf{l}_1}{(2\pi)^2} \int \frac{d^2\mathbf{l}_2}{(2\pi)^2} \int \frac{d^2\mathbf{l}_3}{(2\pi)^2} \langle \kappa(\mathbf{l} - \mathbf{l}_1) \kappa(-\mathbf{l} - \mathbf{l}_2) \kappa(-\mathbf{l}_3) \rangle \\ &\quad \times W(\mathbf{l}_1) W(\mathbf{l}_1 + \mathbf{l}_3) W(\mathbf{l}_3) \exp[-i(\mathbf{l}_1 + \mathbf{l}_2 + \mathbf{l}_3) \cdot \boldsymbol{\theta}_0]. \end{aligned} \quad (2.7)$$

The power spectrum  $P^\kappa$  and the average  $\bar{\kappa}$  used in Eq.(2.7) are estimated from the same patch of the sky. Many such patches are created by dividing the entire survey area. The computation of the average and the power-spectrum from a patch is far simpler than estimating the bispectrum directly. However, it is worth mentioning that such a simplification comes at a price, as the IB can only extract information about the squeezed limit of the bispectrum if we focus on wave numbers  $l$  much larger than the wave numbers that correspond to the fundamental mode of the patch.

Next, we will specialize our discussion for weak lensing surveys. The weak lensing convergence  $\kappa$  is a line-of-sight projection of the 3D density contrast  $\delta(\mathbf{r})$ :

$$\kappa(\boldsymbol{\theta}) := \int_0^{r_s} dr w(r) \delta(r, \boldsymbol{\theta}); \quad w(r) := \frac{3\Omega_M H_0^2}{2} \frac{a^{-1} d_A(r) d_A(r_s - r)}{c^2 d_A(r_s)}. \quad (2.8)$$

Here,  $r$  is the comoving radial distance,  $a$  represents the scale factor,  $H_0$  the Hubble parameter,  $\Omega_M$  the cosmological matter density parameter and  $d_A(r)$  is the comoving angular diameter distance. We will ignore the source distribution and assume them to be localized on a single source plane at a distance  $r = r_s$ , we will also ignore photometric redshift errors. However, such complications are essential to link predictions to observational data and will be included in our analysis in a future publication. Fourier decomposing  $\delta$  along and perpendicular to the line-of-sight direction we obtain:

$$\kappa(\boldsymbol{\theta}) = \int_0^{r_s} dr \omega(r) \int \frac{dk_{\parallel}}{2\pi} \int \frac{d^2\mathbf{k}_{\perp}}{(2\pi)^2} \exp[i(r k_{\parallel} + d_A(r) \boldsymbol{\theta} \cdot \mathbf{k}_{\perp})] \delta(\mathbf{k}; r). \quad (2.9)$$

In our notation,  $k_{\parallel}$  and  $\mathbf{k}_{\perp}$  are the components of the wave vector  $\mathbf{k}$  along and perpendicular to the line-of-sight direction and  $\delta(\mathbf{k})$  is the Fourier transform of the 3D density contrast  $\delta$ .

We have used the following convention for the 3D FT and its inverse:

$$\delta(\mathbf{k}) := \frac{1}{(2\pi)^3} \int d^3\mathbf{x} \exp(-i\mathbf{k} \cdot \mathbf{x}) \delta(\mathbf{x}); \quad \delta(\mathbf{x}) := \int d^3\mathbf{k} \exp(i\mathbf{x} \cdot \mathbf{k}) \delta(\mathbf{k}). \quad (2.10)$$

We have introduced  $\mathbf{x} = (r, \boldsymbol{\theta})$  as the comoving distance and  $\mathbf{k}$  as the corresponding wave number. We will use  $\delta_{3D}$  to denote the 3D Dirac delta function. The 3D power spectrum

and bispectrum for the density contrast  $\delta$  are:

$$\langle \delta(\mathbf{k}_1)\delta(\mathbf{k}_2) \rangle := (2\pi)^3 \delta_{3D}(\mathbf{k}_1 + \mathbf{k}_2) P_{3D}(k_1); \quad k = |\mathbf{k}|; \quad (2.11)$$

$$\langle \delta(\mathbf{k}_1)\delta(\mathbf{k}_2)\delta(\mathbf{k}_3) \rangle := (2\pi)^3 \delta_{3D}(\mathbf{k}_1 + \mathbf{k}_2 + \mathbf{k}_3) B_{3D}(\mathbf{k}_1, \mathbf{k}_2, \mathbf{k}_3). \quad (2.12)$$

Using the Limber approximation the convergence power spectrum  $P^\kappa(k)$  and bispectrum  $B^\kappa(\mathbf{k}_1, \mathbf{k}_2, \mathbf{k}_3)$  can be expressed respectively in terms of the 3D power spectrum  $P_{3D}(k)$  and bispectrum  $B_{3D}(\mathbf{k}_1, \mathbf{k}_2, \mathbf{k}_3)$ :

$$P^\kappa(l) = \int_0^{r_s} dr \frac{\omega^2(r)}{d_A^2(r)} P_{3D}\left(\frac{l}{d_A(r)}; r\right); \quad (2.13a)$$

$$B^\kappa(\mathbf{l}_1, \mathbf{l}_2, \mathbf{l}_3) = \int_0^{r_s} dr \frac{\omega^3(r)}{d_A^4(r)} B_{3D}\left(\frac{\mathbf{l}_1}{d_A(r)}, \frac{\mathbf{l}_2}{d_A(r)}, \frac{\mathbf{l}_3}{d_A(r)}; r\right). \quad (2.13b)$$

The expression for  $B_{3D}$  is deferred until Eq.(2.17). In 2D the angular average of the IB (denoted as  $\bar{B}^\kappa(l)$ ) can be defined as follows:

$$\bar{B}^\kappa(l) := \int \frac{d\varphi_l}{2\pi} B^\kappa(\mathbf{l}); \quad l = |\mathbf{l}|. \quad (2.14)$$

Here  $\varphi_l$  is the angle between the vector  $\mathbf{l}$  and the  $\vartheta$  (R.A.) direction. Next, carrying out the  $\theta_0$  integral in Eq.(2.7) and using the resulting 2D delta function to perform the  $\mathbf{l}_2$  integral leaves us with the following expression:

$$\begin{aligned} \bar{B}^\kappa(\mathbf{l}) &= \int \frac{d\varphi_l}{2\pi} \int \frac{d^2\mathbf{l}_1}{(2\pi)^2} \int \frac{d^2\mathbf{l}_3}{(2\pi)^2} B^\kappa(\mathbf{l} - \mathbf{l}_1, -\mathbf{l} + \mathbf{l}_1 + \mathbf{l}_3, -\mathbf{l}_3) \\ &\quad \times W(\mathbf{l}_1)W(\mathbf{l}_1 + \mathbf{l}_3)W(\mathbf{l}_3). \end{aligned} \quad (2.15)$$

Notice we have also used the definition of the convergence bispectrum in Eq.(2.4). To simplify this further, we will use the following property of the window function  $W$ :

$$W^2(\boldsymbol{\theta}) = W(\boldsymbol{\theta}); \quad W(\mathbf{l}_3) = \int \frac{d^2\mathbf{l}_1}{(2\pi)^2} W(-\mathbf{l}_1 - \mathbf{l}_3)W(\mathbf{l}_1), \quad (2.16)$$

such that in the *squeezed limit* the tree-level perturbative matter bispectrum in the small angle approximation takes the following form [34]:

$$\begin{aligned} &B_{3D}(\mathbf{l}/d_A(r) - \mathbf{l}_1/d_A(r), -\mathbf{l}/d_A(r) + \mathbf{l}_1/d_A(r) + \mathbf{l}_3/d_A(r), -\mathbf{l}_3/d_A(r)) \\ &= \left[ \frac{13}{7} + \frac{8}{7} \left( \frac{\mathbf{l} \cdot \mathbf{l}_3}{l l_3} \right)^2 - \left( \frac{\mathbf{l} \cdot \mathbf{l}_3}{l l_3} \right)^2 \frac{d \ln P_{3D}(l)}{d \ln l} \right] P_{3D}\left(\frac{l}{d_A(r)}\right) P_{3D}\left(\frac{l_3}{d_A(r)}\right) + \dots \end{aligned} \quad (2.17)$$

The terms which are higher-order in terms of  $(l_1/l)$  or  $(l_3/l)$  (where,  $l_i = |\mathbf{l}_i|$ ) are ignored as we take the limiting case that  $l \gg l_i$ . Using the fact that the circular average of  $\mathbf{l} \cdot \mathbf{l}_i/(ll_i)$  is  $[1/2]$  (which is in contrast to the derivation of results applicable in 3D where spherical average of  $\mathbf{l} \cdot \mathbf{l}_i/(ll_i)$  is  $[1/3]$ ), we arrive at the final expression:

$$\bar{B}^\kappa(l) = R_2 \left[ \frac{24}{7} - \frac{1}{2} \frac{d \ln l^2 P_{3D}(l)}{d \ln l} \right] P^\kappa(l) \sigma_L^2; \quad \sigma_L^2 = \langle \bar{\kappa}^2 \rangle; \quad (2.18a)$$

$$R_2 = \int_0^{r_s} dr \frac{w^3(r)}{d_A^{4+2n}(r)} \bigg/ \left( \int_0^{r_s} dr \frac{w^2(r)}{d_A^{2+n}(r)} \right)^2, \quad (2.18b)$$

where we have approximated the power spectrum with a power law  $P_{3D}(k) \propto k^n$ . The normalized IB, denoted as  $\mathcal{B}'(l)$ , is defined as:

$$\mathcal{B}'(l) = \frac{1}{P^\kappa(l)\sigma_L^2} \bar{\mathcal{B}}^\kappa(l) = R_2 \left[ \frac{24}{7} - \frac{1}{2} \frac{d \ln l^2 P_{3D}(l)}{d \ln l} \right]. \quad (2.19)$$

The above expression was derived using tree-level perturbation theory.<sup>10</sup> Using very similar arguments we can show that if we assume a hierarchical *ansatz* for the underlying 3D bispectrum [14]:

$$B_{3D}(\mathbf{k}_1, \mathbf{k}_2, \mathbf{k}_3) = Q_3 [P_{3D}(\mathbf{k}_1)P_{3D}(\mathbf{k}_2) + P_{3D}(\mathbf{k}_2)P_{3D}(\mathbf{k}_3) + P_{3D}(\mathbf{k}_3)P_{3D}(\mathbf{k}_1)]. \quad (2.20)$$

Here,  $Q_3$  is the hierarchal amplitude of three point correlation function which can be computed using Hyperextend Perturbation Theory(HEPT)[35]. The corresponding IB is given by[33]:

$$\bar{\mathcal{B}}^\kappa(l) = 2R_2 Q_3 P^\kappa(l)\sigma_L^2; \quad Q_3 = \frac{4 - 2^n}{1 + 2^{n+1}} \quad (2.21)$$

Here  $n$  denotes the spectral index for the linear 3D power spectrum assumed locally to be power law  $P_{\text{lin}}(k) \propto k^n$ . Similar results in the highly nonlinear regime can also be derived using the halo model, loop level corrections, effective field theory [38], phenomenological fitting functions [39] or separate Universe models [31, 40, 41]. We will not include the primordial non-Gaussianity (of local type [42]) in our analysis but this can also be included as a straight-forward expansion [43]. Most of these theories including the fitting functions can be seen as (physically motivated) interpolation of the results obtained by PT and HEPT which are the two limiting cases.

## 2.2 Zeldovich Approximation

The lowest-order in Lagrangian perturbation theory commonly known as the Zeldovich approximation (ZA) can be used to simplify many aspects of gravitational clustering. Using the same line of analysis as above the IB can be calculated for the ZA. The squeezed bispectrum in this approximation takes the following form:

$$B_{ZA} \stackrel{\text{sq}}{\approx} \left[ 1 + 2 \left( \frac{\mathbf{1} \cdot \mathbf{l}_3}{ll_3} \right)^2 - \left( \frac{\mathbf{1} \cdot \mathbf{l}_3}{ll_3} \right)^2 \frac{d \ln P_{3D}(l)}{d \ln l} \right] P_{3D} \left( \frac{l}{d_A(r)} \right) P_{3D} \left( \frac{l_3}{d_A(r)} \right). \quad (2.22a)$$

Next, going through the expressions outlined in Eq.(2.18a)-Eq.(2.19) we arrive at the corresponding result for the normalized IB using ZA:

$$\mathcal{B}'_{ZA}(l) = R_2 \left[ 3 - \frac{1}{2} \frac{d \ln l^2 P_{3D}(l)}{d \ln l} \right] = R_2 \left[ 3 - \frac{1}{2}(n + 2) \right]. \quad (2.23)$$

The last equality holds only for a power law  $P_{3D}(k)$ . Comparing with Eq.(2.19), we can see that the ZA under predicts the normalized IB. This is consistent with the well-known fact that the normalised skewness parameter  $S_3$  for the ZA is lower than its SPT value [44].

<sup>10</sup>This result is similar to the result obtained in Ref.[37] using a vertex generating function approach. If we identify the second-order vertex  $\nu_2 = 12/7$  computed in Ref.[37] using a 2D spherical dynamics to  $Q_2$ , we get  $\mathcal{B}'(l) = 24/7 R_2$ . Which of course can also be obtained in our approach in the no-smoothing limit, from Eq.(2.19), by substituting  $n = -2$ . However, it is important to realize that despite the formal mathematical similarity the statistics introduced in Ref.[37] or its two-point generalisations and the IB computed here are not the same and their physical interpretation is completely different. Indeed, this formal similarity of mathematical expressions too are only valid at the level of second-order.

### 2.3 Response Function Approach

The (linear) response function approach to IB takes advantage of the fact that the bispectrum in its squeezed configuration can be interpreted as a response of the small scale power spectrum to a long wavelength modulation of  $\bar{\kappa}$ . In this scenario an over(under)dense region is treated as a separate Universe, and the over(under)density is absorbed in a redefinition of the background cosmology. To connect with the response function approach and the modelling used in separate Universe approaches, we expand the convergence power spectrum as follows. We expand the 2D convergence power spectrum estimated from a patch as a function of the average  $\kappa$ , which is a result of the long wavelength fluctuations of the  $\kappa$  field:

$$P^\kappa(l; \boldsymbol{\theta}_0) = P^\kappa(l; \boldsymbol{\theta}_0)|_{\bar{\kappa}(\boldsymbol{\theta}_0)=0} + \frac{dP^\kappa(l; \boldsymbol{\theta}_0)}{d\bar{\kappa}(\boldsymbol{\theta}_0)}\Big|_{\bar{\kappa}(\boldsymbol{\theta}_0)=0} \bar{\kappa}(\boldsymbol{\theta}_0) + \dots \quad (2.24)$$

By correlating  $\bar{\kappa}(\boldsymbol{\theta}_0)$  with  $P^\kappa(l; \boldsymbol{\theta}_0)$  and ignoring terms of  $\mathcal{O}(\bar{\kappa}^3)$  we arrive at the following expression:

$$\bar{\mathcal{B}}^\kappa(l) \equiv \langle \bar{\kappa}(\boldsymbol{\theta}_0) P^\kappa(l; \boldsymbol{\theta}_0) \rangle = \sigma_L^2 \frac{d \ln P^\kappa(l; \boldsymbol{\theta}_0)}{d\bar{\kappa}(\boldsymbol{\theta}_0)} P^\kappa(l; \boldsymbol{\theta}_0); \quad \sigma_L^2 := \langle \bar{\kappa}^2 \rangle. \quad (2.25a)$$

$$\mathcal{B}'(l) = \frac{d \ln P^\kappa(l; \boldsymbol{\theta}_0)}{d\bar{\kappa}(\boldsymbol{\theta}_0)}\Big|_{\bar{\kappa}(\boldsymbol{\theta}_0)=0} \quad (2.25b)$$

The gravity induced bispectrum at tree-level, that we have used above in our derivation given in Eq.(2.17), can be replaced by the primordial bispectrum of inflationary origin (local type [42]) to estimate the corresponding IB. Indeed, the primordial non-Gaussianity is severely constrained by recent data from *Planck* [45, 46], although it is expected that future Stage -IV surveys such as *Euclid* will further tighten such constraints [47]. Similarly results can also be obtained for non-Gaussianity induced by cosmic strings [48]. The generalization of the above result derived for 2D or projected surveys to 3D can be accomplished by cross-correlating  $\bar{\kappa}$  from one redshift bin to the power spectrum estimated from another and vice versa.

Indeed generalization of IB to include external data sets can also be incorporated in a straight-forward manner by cross-correlating the convergence power spectrum in Eq.(2.6) against any other projected field e.g. the tSZ  $y$ -parameter maps, can provide an estimator for the Integrated mixed bispectrum involving  $\kappa$  and  $y$  [33].

### 2.4 All-Sky Formulation

The discussion in the previous section was based on a flat-sky treatment, and indeed many of the recent surveys are small enough so that a flat-sky treatment should be adequate. However, the next generation surveys will cover a considerable fraction of the sky making an all-sky treatment necessary. For a review of all-sky formulations of non-Gaussianity see [42]. Certain aspects of consistency relations for the galaxy bispectrum in the all-sky limit are discussed in [49], and the all-sky versus flat-sky correspondence is analyzed in [50]. We start by defining the spherical harmonic decomposition of the convergence map  $\kappa(\boldsymbol{\theta})$  with and without a mask:

$$\kappa_{\ell m} := \int d^2\boldsymbol{\theta} \kappa(\boldsymbol{\theta}) Y_{\ell m}(\boldsymbol{\theta}); \quad \tilde{\kappa}_{\ell m} := \int d^2\boldsymbol{\theta} W(\boldsymbol{\theta}) \kappa(\boldsymbol{\theta}) Y_{\ell m}(\boldsymbol{\theta}). \quad (2.26)$$



We use  $Y_{\ell m}$  to denote the spherical harmonics of degree  $\ell$  and order  $m$ . The all-sky power spectrum is defined as  $\mathcal{C}_\ell^\kappa = \frac{1}{(2\ell+1)} \sum_m \kappa_{\ell m} \kappa_{\ell m}^*$  and for high- $\ell$  identical to its flat-sky counterparts defined in Eq.(2.3) i.e.  $P^\kappa(l) = \mathcal{C}_l^\kappa$ . In an analogous manner, we introduce the pseudo power spectrum  $\tilde{\mathcal{C}}_\ell^\kappa$ s constructed from the  $\tilde{\kappa}_{\ell m}$ , i.e.  $\tilde{\mathcal{C}}_\ell^\kappa = \frac{1}{(2\ell+1)} \sum_m \tilde{\kappa}_{\ell m} \tilde{\kappa}_{\ell m}^*$ . The angle-averaged bispectrum  $B_{\ell_1 \ell_2 \ell_3}^\kappa$  in spherical harmonic space is:

$$\langle \kappa_{\ell_1 m_1} \kappa_{\ell_2 m_2} \kappa_{\ell_3 m_3} \rangle := \langle B_{\ell_1 \ell_2 \ell_3}^\kappa \rangle \begin{pmatrix} \ell_1 & \ell_2 & \ell_3 \\ m_1 & m_2 & m_3 \end{pmatrix}; \quad (2.27a)$$

$$B_{\ell_1 \ell_2 \ell_3}^\kappa = \sum_{m_i} \begin{pmatrix} \ell_1 & \ell_2 & \ell_3 \\ m_1 & m_2 & m_3 \end{pmatrix} \kappa_{\ell_1 m_1} \kappa_{\ell_2 m_2} \kappa_{\ell_3 m_3}, \quad (2.27b)$$

where the matrix denotes the Wigner  $3j$  symbol. Since  $\ell_1, \ell_2$ , and  $\ell_3$  form a triangle,  $B_{\ell_1 \ell_2 \ell_3}^\kappa$  satisfies the triangle condition,  $|\ell_i - \ell_j| \leq \ell_k \leq \ell_i + \ell_j$  for all permutations of indices; and parity invariance of the angular correlation function demands  $\ell_1 + \ell_2 + \ell_3 = \text{even}$ . For a spherical sky we introduce the reduced bispectrum  $b_{\ell_1 \ell_2 \ell_3}^\kappa$  by the following expression:

$$\langle \kappa_{\ell_1 m_1} \kappa_{\ell_2 m_2} \kappa_{\ell_3 m_3} \rangle = b_{\ell_1 \ell_2 \ell_3}^\kappa \mathcal{G}_{\ell_1 \ell_2 \ell_3}^{m_1 m_2 m_3}; \quad (2.28a)$$

$$\mathcal{G}_{\ell_1 \ell_2 \ell_3}^{m_1 m_2 m_3} := \int d^2\theta Y_{\ell_1 m_1}(\theta) Y_{\ell_2 m_2}(\theta) Y_{\ell_3 m_3}(\theta). \quad (2.28b)$$

this reduced bispectrum  $b_{\ell_1 \ell_2 \ell_3}^\kappa$  is important in deriving the flat-sky limit. The symbol  $\mathcal{G}$  introduced in Eq.(2.28b) is also known as *Gaunt* integral which represents the coupling of three spherical harmonics. To relate Eq.(2.28a) and Eq.(2.4) we note that the Gaunt integral introduced in Eq.(2.28b) becomes a Dirac delta function in the flat-sky limit  $\mathcal{G}_{\ell_1 \ell_2 \ell_3}^{m_1 m_2 m_3} \approx (2\pi)^2 \delta_{2D}(\mathbf{l}_1 + \mathbf{l}_2 + \mathbf{l}_3)$ , which leads us to identify the reduced bispectrum as the flat-sky bispectrum [50]:  $b_{\ell_1 \ell_2 \ell_3}^\kappa \approx B^\kappa(\mathbf{l}_1, \mathbf{l}_2, \mathbf{l}_3)$ ; and similarly Eq.(2.30) and Eq.(2.29).

Next, to define the IB we will introduce a mask or a window  $W(\boldsymbol{\theta}, \boldsymbol{\theta}_0)$  whose harmonics are defined by  $W_{\ell m}(\boldsymbol{\theta}_0) = \int d^2\theta W(\boldsymbol{\theta}, \boldsymbol{\theta}_0) Y_{\ell m}(\boldsymbol{\theta})$ . Individual patches are identified with specific value of  $\boldsymbol{\theta}_0$ . However, to simplify notation, we will suppress the  $\boldsymbol{\theta}_0$  dependence in  $W_{\ell m}$  and the resulting coupling matrix  $M$  defined below. The all-sky harmonics and their partial sky counterparts are related through a coupling matrix  $M$  [51]:

$$\tilde{\kappa}_{\ell_1 m_1} = \sum_{\ell_2 m_2} M_{\ell_1 m_1, \ell_2 m_2} \kappa_{\ell_2 m_2}; \quad M_{\ell_1 m_1, \ell_2 m_2} = \sum_{\ell m} W_{\ell m} \mathcal{G}_{\ell_1 \ell_2 \ell}^{m_1 m_2 m}. \quad (2.29)$$

Using the flat-sky convention introduced in Eq.(2.2) the flat-sky equivalent of Eq.(2.29) takes the following form:

$$\tilde{\kappa}(\mathbf{l}_1) = \int d^2\mathbf{l}_2 M_{\mathbf{l}_1 \mathbf{l}_2} \kappa(\mathbf{l}_2); \quad M_{\mathbf{l}_1 \mathbf{l}_2} = \int d^2\mathbf{l} W(\mathbf{l}) \delta_{2D}(\mathbf{l} + \mathbf{l}_1 - \mathbf{l}_2). \quad (2.30)$$

Here,  $M_{\mathbf{l}_1 \mathbf{l}_2}$  is the flat-sky counterpart of  $M_{\ell_1 m_1, \ell_2 m_2}$ .

To construct an all-sky estimator we use the fact that the average of  $\kappa$  over a region  $\bar{\kappa}$  is given by the monopole  $\kappa_{00}$ :  $\bar{\kappa} = \tilde{\kappa}_{00} = \sum_{\ell_1 m_1} M_{00, \ell_1 m_1} \kappa_{\ell_1 m_1}$ . The estimator for the IB is formed by cross-correlating the pseudo power spectrum, denoted as  $\tilde{\mathcal{C}}_\ell^\kappa$ , with  $\bar{\kappa}$ :

$$\begin{aligned} \bar{\mathcal{B}}_\ell^\kappa &:= \langle \bar{\kappa} \tilde{\mathcal{C}}_\ell \rangle = \frac{1}{2\ell+1} \sum_m \langle \tilde{\kappa}_{00} \tilde{\kappa}_{\ell m} \tilde{\kappa}_{\ell m}^* \rangle \\ &= \frac{1}{2\ell+1} \sum_m \sum_{\ell_i m_i} \begin{pmatrix} \ell_1 & \ell_2 & \ell_3 \\ m_1 & m_2 & m_3 \end{pmatrix} M_{\ell m, \ell_1 m_1} M_{\ell m, \ell_2 m_2} M_{00, \ell_3 m_3} B_{\ell_1 \ell_2 \ell_3}^\kappa \end{aligned} \quad (2.31)$$

Next, using the correspondence discussed between flat-sky and all-sky before, it is straightforward to show that in the limit of high- $\ell$  this reduces to the 2D estimator in Eq.(2.15).

We have focused on the convergence  $\kappa$  which is a spin-0 or a scalar field. Similar results can be obtained by using an E/B decomposition of shear maps [52, 53] and corresponding squeezed EEE and BBB bispectra; these results will be presented elsewhere. Finally, many Bayesian estimators have been recently developed for power-spectrum analysis e.g. [54, 55]; using such an estimator for  $\mathcal{C}_\ell^\kappa$  in Eq.(2.31) would pave the way for the development of the first Bayesian estimation of the bispectrum.

### 3 Analytical Modelling of IB

In this section we will introduce different approaches that we will use for the theoretical prediction of the IB. Indeed, a detailed understanding of gravitational clustering in the nonlinear regime is lacking, though is of paramount importance for cosmology, nevertheless these approximations should be considered only as an illustrative proxy for the true system exhibiting much richer dynamics.

#### 3.1 Halo Model

The ‘halo model’ [56] is arguably the most popular model for predicting the clustering properties of dark matter. It is a phenomenological model that is based on the assumption that all matter is contained within spherical halos of properties that are completely determined by their mass distribution, radial profile and clustering properties. Variants of the halo model, used to predict dark matter clustering, differ in fine detail with respect to these ingredients. Using the small-angle approximation the halo model can be encapsulated by:

$$P_{3\text{D}}(k_\perp, a) = P^{1\text{h}}(k_\perp, a) + P^{2\text{h}}(k_\perp, a); \quad (3.1)$$

$$P^{2\text{h}}(k_\perp, a) = [I_1^1(k_\perp)]^2 P_{\text{lin}}(k_\perp, a); \quad P^{1\text{h}}(k_\perp, a) = I_2^0(k_\perp, k_\perp); \quad (3.2)$$

$$\begin{aligned} \frac{dP_{3\text{D}}(k_\perp, a)}{d\bar{\delta}} \Big|_{\bar{\delta}=0} &= \left[ \left( \frac{24}{7} - \frac{1}{2} \frac{d \ln k_\perp^2 P(k_\perp, a)}{d \ln k_\perp} \right) P^{2\text{h}}(k_\perp, a) \right. \\ &\quad \left. + 2I_1^2(k_\perp) I_1^1(k_\perp) P_{\text{lin}}(k_\perp, a) + I_2^1(k_\perp, k_\perp) \right]. \end{aligned} \quad (3.3)$$

As before we use the small angle approximation i.e.  $k_\perp \gg |k_\parallel|$  where  $k_\parallel$  and  $\mathbf{k}_\perp$  are components parallel and perpendicular to the line-of-sight. Where,  $P^{1\text{h}}$  and  $P^{2\text{h}}$  are the one- and two-halo contributions to the total power spectrum  $P_{3\text{D}}(k, a)$  at a redshift  $z$ ,  $a = 1/(1+z)$  and wavenumber  $k$ . The nonlinear power spectrum  $P_{3\text{D}}(k, a)$  depends on the linear power spectrum  $P_{\text{lin}}(k, a)$  through the two halo contribution. We have also used the following notation in Eq.(3.2)-Eq.(3.3):

$$I_m^n(k_{1\perp}, \dots, k_{m\perp}) := \int d \ln M n(\ln M) \left( \frac{M}{\rho} \right)^m b_n(M) \Pi_{i=1}^m u(M|k_{i\perp}), \quad (3.4)$$

where  $u(M|k)$  is the Fourier transform of the halo radial profile. The (higher-order) bias functions  $b_N$  for halos of mass  $M$  that appear in Eq.(3.4) are defined as a response of the halo number density  $n(\ln M)$  to change in  $\bar{\delta}$  (average density contrast in a finite patch):

$$b_N(M) := \frac{1}{n(\ln M)} \frac{\partial^N n(\ln M)}{\partial \bar{\delta}^N}. \quad (3.5)$$

We can use Eq.(3.3) in Eq.(2.24) to compute the IB. Using these ingredients we can finally write the normalised IB in the halo model as:

$$\mathcal{B}'(l) := \frac{1}{P^\kappa(l)} \frac{dP^\kappa}{d\bar{\kappa}} = \frac{1}{|\kappa_{\min}|P^\kappa(l)} \int \frac{w^2(r)}{d_A^2(r)} \frac{d}{d\bar{\delta}} P_{3D} \left( \frac{l}{d_A(r)}; r \right); \quad (3.6a)$$

$$\kappa_{\min} = - \int_0^{r_s} dr w(r). \quad (3.6b)$$

In our above evaluation, we have used the mapping  $\delta \rightarrow \kappa/|\kappa_{\min}|$  to arrive at  $\bar{\delta} \rightarrow \bar{\kappa}/|\kappa_{\min}|$  (see Appendix-§A for more detailed discussion) which gives  $d/d\bar{\kappa} = 1/|\kappa_{\min}|d/d\bar{\delta}$ . We have also implicitly assumed that  $\bar{\delta}$  only changes the power spectrum not the geometry e.g.  $d_A(r)$  and the lensing kernel  $w(r)$ . Evaluation of the power spectrum in the halo model is done using Eq.(3.1) in association with Eq.(2.13a). The derivative of the power spectrum is given in Eq.(3.3). If we ignore the last two terms in Eq.(3.3) we will recover the perturbative results in Eq.(2.18a) and Eq.(2.18b).

### 3.2 Effective Field Theory (EFT)

The EFT is based on incorporating small-scale effects where standard perturbations theory (SPT) fails [57, 58]. This is done through exploitation of symmetries inherent in the system by modifying the ideal fluid description to a non-ideal fluid through inclusion of counter-terms that are related to non-zero pressure, viscosity and thermal conductivity terms. This also alleviates the UV divergent integrals that appear at loop level in SPT which often dominate their high- $k$  behavior. This leads to inclusion of additional parameters that are calibrated using numerical simulations. The bispectrum in the EFT was recently discussed in [59] (see [38] for more detailed discussion and complete list of references).

For defining the squeezed limit of the 3D bispectrum we will follow the following notation:

$$B_{3D}(\mathbf{k}_1, \mathbf{k}_2, \mathbf{k}_3) \stackrel{\text{sq}}{\approx} \lim_{\mathbf{q}_1, \mathbf{q}_3 \rightarrow 0} B_{3D}(\mathbf{k} - \mathbf{q}_1, -\mathbf{k} + \mathbf{q}_1 + \mathbf{q}_3, -\mathbf{q}_3). \quad (3.7)$$

We have used the parametrization  $\mathbf{k}_1 = \mathbf{k} - \mathbf{q}_1$ ,  $\mathbf{k}_2 = -\mathbf{k} + \mathbf{q}_1 + \mathbf{q}_3$  and  $\mathbf{k}_3 = -\mathbf{q}_3$  and taken the limit  $\mathbf{q}_1, \mathbf{q}_3 \rightarrow 0$  to recover the squeezed limit [38]. The superscript sq above represents the squeezed limit. Various contributions to the EFT bispectrum are listed below:

$$B_{2D}^{\text{EFT}} = B_{2D}^{\text{SPT}} + B_{\delta_c^{(1)}} + B_{\delta_c^{(2)}, \delta} + B_{\delta_c^{(2)}, e} + B_{\delta_c^{(2)}, \alpha\beta}, \quad (3.8)$$

where the arguments to various  $B$  terms have been suppressed for clarity. The various terms that contribute to bispectrum at the squeezed limit are then as follows [38]:

$$B_{2D}^{\text{SPT}} \stackrel{\text{sq}}{\approx} \left[ \frac{17}{7} - \frac{n}{2} \right] P_{3D}(k_\perp) P_{3D}(q_{3\perp}), \quad (3.9)$$

$$B_{\delta_c^{(1)}} \stackrel{\text{sq}}{\approx} -\xi \left[ \frac{20 - 7n}{14} \right] k_\perp^2 P_{3D}(k_\perp) P_{3D}(q_{3\perp}), \quad (3.10)$$

$$B_{\delta_c^{(2)}, \delta} \stackrel{\text{sq}}{\approx} -\xi M_d \left[ \frac{48 - 7n}{14} \right] k_\perp^2 P_{3D}(k_\perp) P_{3D}(q_{3\perp}), \quad (3.11)$$

$$B_{\delta_c^{(2)}, e} \stackrel{\text{sq}}{\approx} -\xi M_d \left[ 4 \frac{\epsilon_1}{\xi} + \frac{2}{3} \frac{\epsilon_2}{\xi} + \frac{1}{3} \frac{\epsilon_3}{\xi} \right] k_\perp^2 P_{3D}(k_\perp) P_{3D}(q_{3\perp}), \quad (3.12)$$

$$B_{\delta_c^{(2)}, \alpha\beta} \stackrel{\text{sq}}{\approx} -\xi \frac{2 \left[ (56 + 44m_d + 8m_d^2) - (11 + 4m_d)n \right]}{(2 + m_d)(9 + 2m_d)} k_\perp^2 P_{3D}(k_\perp) P_{3D}(q_{3\perp}). \quad (3.13)$$

We have used the small-angle approximation in our derivation. As before, we have assumed a power-law power spectrum  $P_{3D}(k) \propto k^n$ . To connect with results derived using SPT in §2.1 we use  $k_\perp = l/d_A(r)$  and  $q_{3\perp} = l_3/d_A(r)$  and perform the line-of-sight integration similar to Eq.(2.15). We will take  $\xi = [1.5 \pm 0.03]h^{-2}\text{Mpc}^2$  [59] which is the scale at which EFT contributions start to dominate and  $m_d$  is related to the temporal evolution of EFT contribution assumed to be  $\propto D_+^{m_d}$  ( $D_+$  being the linear growth factor) and  $M_d$  is defined as:

$$M_d := \left[ \frac{(m_d + 1)(2m_d + 7)}{(m_d + 2)(2m_d + 9)} \right], \quad (3.14)$$

where

$$\frac{\epsilon_1}{\xi} = \frac{3466}{14091}, \quad \frac{\epsilon_2}{\xi} = \frac{7285}{32879}, \quad \frac{\epsilon_3}{\xi} = \frac{41982}{52879}. \quad (3.15)$$

Here the counter-terms added to the SPT results are denoted by the superscript SPT. The final expression for the normalised IB takes the following form:

$$\mathcal{B}'(l) = \mathcal{B}'_{\text{SPT}}(l) + R_2^{\text{EFT}} l^2 \xi \mathcal{B}'_{\text{EFT}}(l) \quad (3.16a)$$

$$R_2^{\text{EFT}} := \int_0^{r_s} dr \frac{w^3(r)}{d_A^{6+2n}(r)} \bigg/ \left( \int_0^{r_s} dr \frac{w^2(r)}{d_A^{2+n}(r)} \right)^2, \quad (3.16b)$$

$$\begin{aligned} \mathcal{B}'_{\text{EFT}}(l) := & - \left[ \frac{20 - 7n}{14} \right] - M_d \left[ \frac{48 - 7n}{14} \right] - M_d \left[ 4 \frac{\epsilon_1}{\xi} + \frac{2}{3} \frac{\epsilon_2}{\xi} - \frac{1}{3} \frac{\epsilon_3}{\xi} \right] \\ & - \frac{2 [(56 + 44m_d + 8m_d^2) - (11 + 4m_d)n]}{(2 + m_d)(9 + 2m_d)}. \end{aligned} \quad (3.16c)$$

The SPT value for  $\mathcal{B}'$  computed in Eq.(2.18a) is being denoted here as  $\mathcal{B}'_{\text{SPT}}$ . The prefactor  $R_2$  is defined in Eq.(2.18b) and its numerical values are tabulated in Table-1. As explained before, this result depends crucially on the assumption of locally power-law power spectrum with index  $n$ . Using a dimensional analysis of Eq.(3.16c) can show that the corrections from EFT to SPT scales typically as  $-\xi l^2/[d_A^2|\kappa_{\min}|]$ . The origin of  $\kappa_{\min}$  in the correction term stems from using the approximation discussed in Appendix-§A.

Notice that the parameters defined above can not be computed within the EFT framework. They are estimated using numerical simulations. Currently these parameters are known only for  $z = 0$  and are expected to be valid upto  $k \approx 0.22h\text{Mpc}^{-1}$ . Derivation of the above expressions also require the assumptions of self-similarity and the EdS (Einstein-de Sitter) parameter  $m_d$  is fixed at  $m_d = 5/3$ . A different value of  $m_d = 1$  is also considered. It is generally assumed that these numerical values will continue to hold for other cosmologies i.e. for values of  $M_d$  that we will use in our calculation,  $m_d = 1$  and  $m_d = (1 - n)/(3 + n)$  where  $n$  is the slope of linear power spectrum. However, due to lack of accurate values of the parameters a line-of-sight integration can not be performed, though a crude estimate for a given source redshift can be obtained by using the squeezed expressions in a line-of-sight integration in association with the small-angle approximation introduced before to match the perturbative results at low  $\ell$ . Here  $B_{2D}^{sq}$  is the 2D bispectrum in the *squeezed* limit. To separate the projection effect from the dynamical effect we also define a 2D IB and its normalised

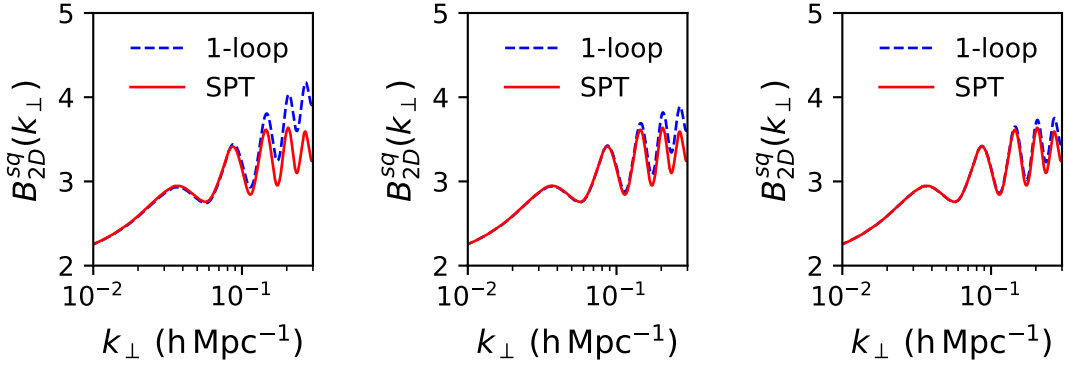


**Figure 1:** The normalised 2D IB  $B_{2D}^{sq}(k_{\perp})$  defined in eq.(3.17b) is plotted as a function of the wave-number  $k_{\perp}$  for SPT. From left to right we show redshifts  $z = 0, 1$  and  $2$ . The expression for one loop correction is give in Eq.(3.19)

counterpart as below:

$$\bar{B}_{2D}(k_{\perp}) = B_{2D}^{sq}(k_{\perp})P_{3D}(k_{\perp})\sigma_{2D}^2; \quad \sigma_{2D}^2 := \frac{1}{2\pi} \int q_{3\perp} dq_{3\perp} P_{3D}(q_{3\perp}); \quad (3.17a)$$

$$B_{2D}^{sq}(k_{\perp}) := \frac{1}{P_{3D}(k_{\perp})\sigma_{2D}^2} \bar{B}_{2D}(k_{\perp}). \quad (3.17b)$$

Comparing this result with Eq.(2.19) we can check that except the factor of  $R_2$ ,  $B_{2D}^{sq}$  is identical to  $\mathcal{B}'$ . The geometric effect is encoded in  $R_2$  and results from line-of-sight projection.

### 3.3 Linear Response Function and Separate Universe Approach

The response function is typically used in conjunction with a separate Universe approach [60–63]. In the separate Universe approach, the coupling of small-wavelength and long wavelength modes are treated by assuming each sub volume (sub-patches) actually evolves as a separate Universe. This approach has been used in various contexts [31, 40, 41]. The modulation in background density due to long wavelength perturbation is absorbed in the redefinition of the background density. This formalism when combined with the perturbative approach results in the following expressions [14]:

$$P_{3D}(k, a) = P_{\text{lin}}(k, a) + 2P_{13}(k, a) + P_{22}(k, a) + \dots; \quad (3.18)$$

$$P_{22}(k, a) = 2 \int \frac{d^3\mathbf{q}}{(2\pi)^3} P_{\text{lin}}(q, a) P_{\text{lin}}(|\mathbf{k} - \mathbf{q}|, a) [F_2(\mathbf{q}, \mathbf{k} - \mathbf{q})]^2; \quad (3.19)$$

$$P_{31}(k, a) = 6 \int \frac{d^3\mathbf{q}}{(2\pi)^3} P_{\text{lin}}(k, a) P_{\text{lin}}(q, a) [F_3(\mathbf{q}, \mathbf{k}, -\mathbf{q})]^2. \quad (3.20)$$

The kernels  $F_2$  and  $F_3$  introduced above encapsulates mode coupling at second and third order in perturbation theory (for more discussion about the kernels  $F_2, F_3$  as well as their higher order counterparts and related recursion relation see ref.[14]). The response function

**Table 1:** The normalized IB defined in Eq.(2.19) as a function of spectral index  $n$  and source redshift  $z_s$ . We have used the SPT prescription valid at low values of  $\ell$  presented in Eq.(2.19) to compute the IB.

	$n = -1.0$	$n = -1.5$	$n = -2.0$
$z_s = 0.5$	406	407	442
$z_s = 1.0$	112	114	124
$z_s = 1.5$	56	58	64
$z_s = 2.0$	36	37	41

can be expressed using the linear power spectrum  $P_{\text{lin}}(k, a)$  and the loop level corrections  $P_{13}(k, a)$  and  $P_{22}(k, a)$  as follows:

$$\frac{d \ln P_{3\text{D}}(k_{\perp}, a)}{d\bar{\delta}} = \frac{24}{7} - \frac{1}{2} \frac{d \ln k_{\perp}^2 P_{\text{lin}}(k_{\perp}, a)}{d \ln k_{\perp}} + \frac{10}{7} \frac{2P_{13}(k_{\perp}, a) + P_{22}(k_{\perp}, a)}{P_{3\text{D}}(k_{\perp}, a)} \quad (3.21)$$

The above expression includes loop-level correction at one loop but can be improved by including higher-order loop terms. However, the entire perturbative series fails to converge at smaller scales and lower redshifts where the variance is comparable to unity. In this case a nonlinear fitting function is typically used which reproduces the numerical simulations (e.g. [64]). Indeed, such fitting functions, in general, do not provide an insight to the response to changes in cosmological parameters. The response function in terms of nonlinear power spectrum has the following form:

$$\frac{d \ln P_{3\text{D}}(k_{\perp}, a)}{d\bar{\delta}} = 2 + \frac{10}{7} \frac{d \ln P_{3\text{D}}(k_{\perp}, a)}{d \ln \sigma_8} - \frac{1}{2} \frac{d \ln k_{\perp}^2 P_{3\text{D}}(k_{\perp}, a)}{d \ln k_{\perp}}. \quad (3.22)$$

Substituting  $dP_{3\text{D}}/d\bar{\delta}$  from Eq.(3.22) or Eq.(3.21) in Eq.(3.6a-3.6b) we can compute the IB in these approaches as discussed in §3.1 in the context of halo model. Indeed, it is possible to replace  $F_2$  in Eq.(3.19) with an effective  $F_2^{\text{eff}}$  that is effectively a fitting function to numerical simulation [39, 65].

The results of comparison of SPT predictions and 1-loop corrections are presented in Figure-1. Similar results for SPT and EFT are shown in Figure-2.

## 4 *Euclid* Flagship Simulations

The simulations that we use are discussed in [66] (also see [67, 68]<sup>11</sup>). The flagship mock pipeline will be described in [69]. The basic method used for the assignment of galaxies to halos in the Flagship mock is detailed in [70].

The cosmological parameters used for this simulation are:  $\Omega_{\text{M}} = 0.319$ ,  $\Omega_b = 0.049$ ,  $\Omega_{\text{CDM}} = 0.270$ ,  $\Omega_{\Lambda} = 0.681$ ,  $h = 0.67$ ,  $\sigma_8 = 0.83$ ,  $n_s = 0.96$ ,  $N_{\text{eff}} = 3.046$  and  $M_{\nu} = 0$ . The Box Size used was  $3.78h^{-1}\text{Gpc}$ . A Particle Grid with  $12600^3$  (2 trillion) particles was used with softening length  $6h^{-1}\text{kpc}$ . The particle mass that was used is  $2.39 \times 10^9 h^{-1}M_{\odot}$ . The simulations were started at a redshift of  $z_{\text{Start}} = 49$  and a 2nd-order Lagrangian Perturbation

<sup>11</sup>Flagship Simulations

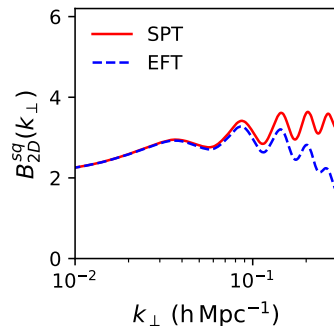


**Figure 2:** The 2D squeezed bispectrum defined in eq.(3.17b) is plotted as a function of projected wave number (2D)  $k_{\perp}$ .

Theory was used for initial particle displacement. The CAMB<sup>12</sup> transfer function was set at  $z = 0$ . It took runtime of 80 hours on 4000 Nodes (8 core + K20X GPU). A total of 11 Snapshots of compressed outputs between  $z = 0.76$  and 0.0 (154 TB) were taken that were used for our study. We note that for the analysis presented here, we have degraded the original HEALPix maps to a lower resolution,  $N_{\text{side}} = 2048$  which corresponds to a pixel scale of 1.7 arcmin. The square patches generated for our study were created using a rectangular grid and interpolating the value of the convergence map from the nearest HEALPix pixel. Few examples of convergence maps generated for our study are presented in Figure -3 and Figure -4.

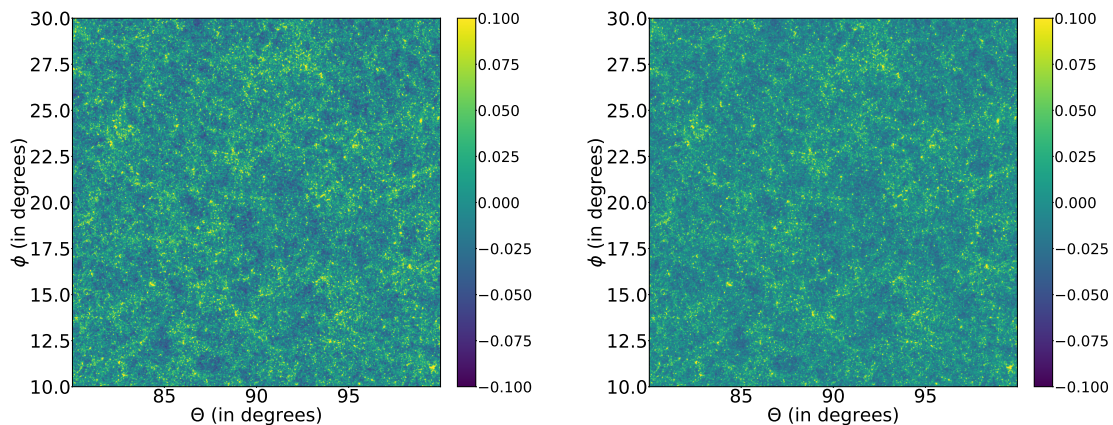


**Figure 3:** The convergence  $\kappa$  maps on 2D patches of the sky generated using the all-sky Flagship Euclid simulations are presented. The patches are  $20^{\circ} \times 20^{\circ}$  in size and are created on a grid  $1024 \times 1024$  grid. The original all-sky maps were generated using  $\ell_{\text{max}} = 2N_{\text{side}}$  with  $N_{\text{side}} = 2048$ . Two different panels correspond to different source redshifts. The left panel correspond to  $z = 0.5$  and the right panel correspond to  $z = 1.0$  (see text for more details).

<sup>12</sup>CAMB

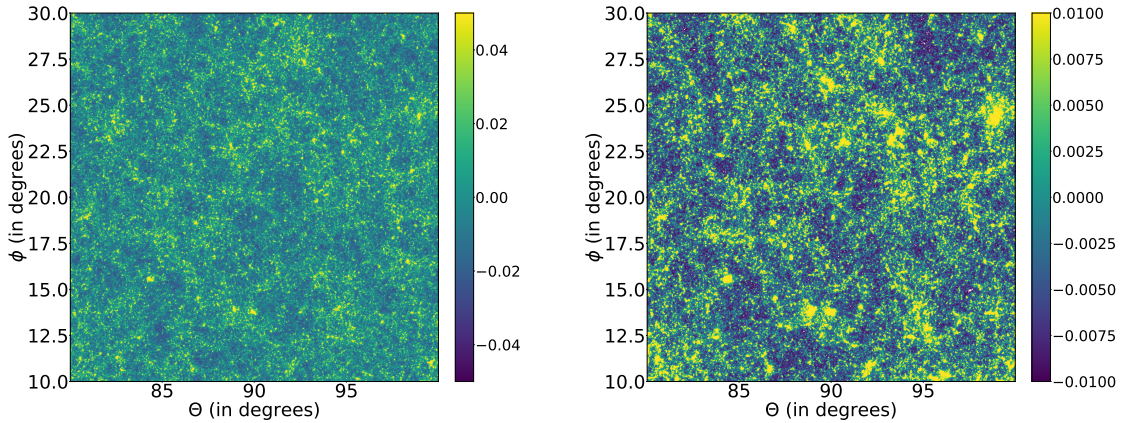


**Figure 4:** Same as Figure-3. The left (right) panel corresponds to  $z = 1.5(2.0)$ .

## 5 Error Budget for IB

### 5.1 Bias

The finite volume of a survey makes the estimators of the higher-order correlation functions or the associated spectra biased. In case of two-point correlation function (or equivalently the Power Spectrum), this is also known as the *integral constraint*. In the weakly non-linear regime this is directly proportional to average of the two-point correlation function  $\bar{\xi}_2(L)$ . At smaller scales, correction term also depends on the squeezed limit of the very bispectrum (convolved with survey window) which we are trying to estimate (see Eq.(413) in ref.[14]). Such corrections however play an important role in estimation of the IB at low redshift e.g.  $z = 0.5$ . An iterative method is required to model the correction coming from finite volume of the survey. A detailed analysis will be presented elsewhere.

### 5.2 Scatter

Estimations of bispectra and its covariance are rather difficult to compute as they are functions of three different wave vectors that define a specific triangular configuration. The estimation of bispectra for all possible triangular configuration can be expensive. The IB on the other hand involves only wave vectors as it focuses only on the squeezed limit of the bispectrum. However, quantifying bispectrum and its covariance in the squeezed limit probes coupling of short and long wavelength modes. Direct evaluations of bispectra in the squeezed limit require simulations with high dynamical range, which can resolve both high and low wave numbers reasonably well. In general separate universe models are implemented where the long wave fluctuations are absorbed in the background evolution with a modified cosmology which allows smaller boxes to be used for resolving the small wavelength modes independently.

The covariance calculation we employ here is a simple order of magnitude calculation based on the counting of modes based on the survey size, and the smaller patches created from it. For the purposes of covariance estimation it is assumed that the underlying distribution is Gaussian. If we take a 2D survey (simulation) with an area denoted as  $A_s$  and focus on patches of area  $A_p$ . the number of patches is  $N_p = \sqrt{A_s/A_p}$ . The number of Fourier modes



in the interval  $(\mathbf{l} - \Delta\mathbf{l}/2)$  and  $(\mathbf{l} + \Delta\mathbf{l}/2)$  is denoted as  $N_L$ . The variance of the convergence bispectrum defined in Eq.(2.18a) is defined as:

$$\sigma^2[B^\kappa(\mathbf{l})] = \langle [B^\kappa(\mathbf{l}) - \langle B^\kappa(\mathbf{l}) \rangle]^2 \rangle = \langle B^\kappa(\mathbf{l})^2 \rangle - \langle B^\kappa(\mathbf{l}) \rangle^2 \quad (5.1a)$$

$$\sigma^2[B^\kappa(\mathbf{l})] = \frac{A_p}{A_s N_{kL}} \sigma_L^2 [P_L^\kappa(\mathbf{l})]^2 \quad (5.1b)$$

The variance of the normalized bispectrum defined in Eq.(2.19) on the other hand is given by:

$$\sigma^2[\mathcal{B}^\kappa(\mathbf{l})] = \frac{A_p}{A_s N_L} \frac{1}{\sigma_L^2}, \quad (5.1c)$$

where we have introduced the following quantities:

$$\sigma_L^2 := \frac{1}{V^2} \int \frac{d^2\mathbf{l}}{(2\pi)^2} P_{lin}^\kappa(\mathbf{l}) |W(\mathbf{l})|^2; \quad (5.1d)$$

$$P_L^\kappa(\mathbf{l}) := \frac{1}{V^2} \int \frac{d^2\mathbf{l}'}{(2\pi)^2} P_{lin}^\kappa(\mathbf{l}') W(|\mathbf{l} - \mathbf{l}'|). \quad (5.1e)$$

$P_L^\kappa(\mathbf{l})$  is the power-spectrum convolved with window for the sub-patches. The above derivations ignore all higher-order correlations. The expression in Eq.(5.1c) is derived assuming the scatter is completely dominated by the scatter in bispectrum.

## 6 Results and Discussion

We present results of the numerical evaluation of the IB from simulated maps. This is done by first dividing the all-sky maps into non-overlapping square patches; the next step is to cross-correlate the power spectrum estimated from these patches with the average convergence  $\bar{\kappa}$  from these patches. In our study, we have considered 18 sub-divisions in the longitudinal  $\theta$  direction and 9 sub-divisions in the azimuthal  $\phi$  direction where the center of the individual patches are placed i.e.  $\theta_S = 10^\circ$  and  $\phi_S = 10^\circ$ . The Euclid flagship all-sky maps were constructed at a resolution specified by the HEALPix<sup>13</sup> resolution parameter  $N_{\text{side}} = 2048$ . We have considered various degradations to  $N_{\text{side}} = 1024$  and  $N_{\text{side}} = 512$  to ascertain the pixelisation error. The square patches were constructed at  $1024 \times 1024$  as well as  $512 \times 512$  to investigate any residuals originating from mapping from all-sky to patch-sky. We have considered convergence maps at four different redshifts  $z_s = 0.5, 1.0, 1.5$  and  $2.0$ . For estimation of the power spectrum, we have taken the minimum and maximum value of harmonics to be  $\ell_{\text{min}} = 200$  and  $\ell_{\text{max}} = 2000$  with 30 logarithmic bins. These choices are dictated by the patch size and pixel size. The results of our analysis for various redshifts are shown respectively in Figure -5, Figure -6, Figure -7 and Figure -8. We have compared the theoretical expectations from SPT against the results from simulations. For the highest redshift maps the detection of non-Gaussianity is dominated by the variance of the IB estimator and lower redshift they are dominated by finite (volume) size effect.

We summarise our observations here:

- **Finite size of the catalog:** At low redshift, the non-Gaussianity is more pronounced hence effects due to finite size of the map bias the estimates. This effect has been

---

<sup>13</sup>Healpix

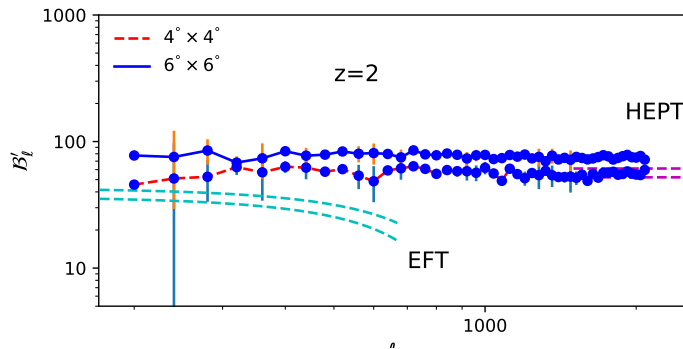


**Figure 5:** We show the estimated IB or  $\mathcal{B}'_\ell$  defined in Eq.(2.19) as a function of the multipoles  $\ell$ . A total of 30 logarithmic bins were used to estimate the bispectrum. The red (blue) dots represent a box-size of  $4^\circ(6^\circ)$ . A total of more than 350 patches were used. The original all-sky map was degraded from  $N_{\text{side}} = 2048$  to  $N_{\text{side}} = 1024$ . The 2D patch-sky maps were constructed on a  $1024 \times 1024$  grid. We do not include noise. The convergence map considered for this plot corresponds to a redshift of  $z = 2.0$ . The error-bars were constructed from approximately 300 patches created for our study. The dashed-lines shown at low  $\ell$  are the predictions from EFT for spectral slope of  $n = -1.5$  (bottom curve) and  $-2.0$  (top curve) as tabulated in Table-1. The dashed lines at high- $\ell$  are predictions from HEPT with exactly the same spectral slope. We have truncated the EFT predictions when they become 50% of the SPT predictions as they are developed at 1-loop and not likely to be valid beyond this point. The HEPT is not expected to be valid at low  $\ell$  which probes mainly the quasi-linear regime (see text for more details).

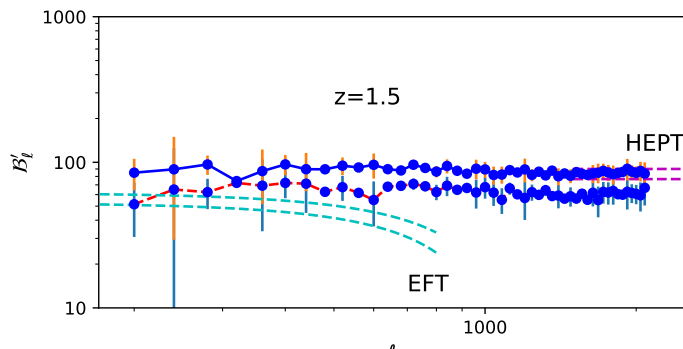


**Figure 6:** Same as Figure-5 but for  $z_s = 1.5$ . Notice that the value of the normalized IB increases with decrease in source redshift  $z_s$ . This is due to the increase in the value of  $R_2$  defined in Eq.(2.18b). We show results for  $\ell \geq 200$  as for smaller values of  $\ell$ , corrections due to the departure from the Limber approximation, used in our derivation, can no longer be ignored.

studied in great detail in the literature for other non-Gaussianity estimators namely the lower-order one-point and two-point cumulants and their correlators [71–73]. The IB probes the same underlying statistics as skewness namely the bispectrum. Thus, it

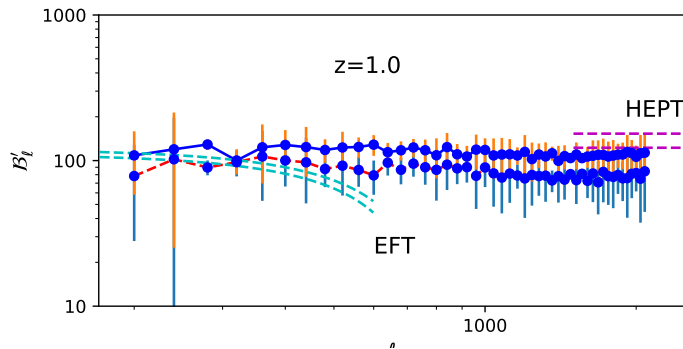


**Figure 7:** Same as Figure-5 but for  $z_s = 1.0$ . The range of  $\ell$  for which the EFT is valid decreases with decrease in source redshift  $z_s$  as the light rays encounter higher level of non-linearity at all scales. Due to the lack of formal derivation of validity range of EFT, we have plotted the EFT predictions till its value becomes comparable to 50% of the SPT predictions. Indeed this also depends on the values of the EFT parameters being used.

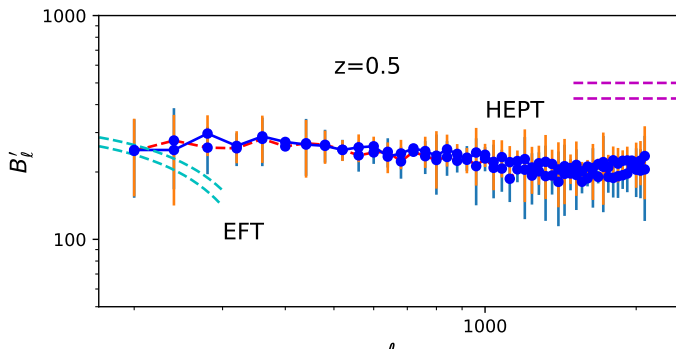


**Figure 8:** Same as Figure-5 but for  $z_s = 0.5$ . At this particular source redshift the light rays which are being lensed are probing highly nonlinear regime. This means the range of validity of EFT is rather limited. Indeed, the bias introduced by the finite size of the map are more pronounced too. In addition the theoretical predictions are lot more sensitive to the source redshift  $z_s$ . These effects combine to make comparison of theoretical predictions and numerical estimates from simulations rather difficult.

is expected, that it too will be affected by finite size of a catalog in a similar manner. It can be reduced by increasing the size of the catalog. However, correction to the small angle approximation needs to be included in analysing low- $\ell$  estimates from such patches. Indeed, such an effect also depends on the level of non-linearity. So, corrections are more pronounced at lower redshift ( $z_s = 0.5$ ) where convergence maps are more nonlinear compared to the ones at higher redshift ( $z_s = 2.0$ ). This results in a larger deviation from theoretical (SPT) predictions in Figure -8. We have not generalized the available methods in the literature [14] to *correct* the bias in our estimates at low  $z$  which is left to a future work. Most current results concern one-point statistics in real

space.

The corrections from the curvature of sky start play an increasingly dominant role for  $\ell < 100$  [74–76]. To ensure that our results are not affected by any deviation from flat-sky approximation we have only considered the results for  $\ell > 200$ .

- **Approximate window function:** We have presented our results for two different patch sizes to investigate the effect of the *window function*. Our numerical results were evaluated using a square patch while the theoretical results were derived using a circular window. Such effects are more visible at higher redshifts as the underlying non-Gaussianity is relatively low. It is possible to include a circular window when analysing the maps or include the effect by direct integration when computing theoretical predictions. However, this will not change the results at a fundamental level.
- **Sample variance and error-bars:** To have crude estimates of error bars, we have used the patches generated for our study. We haven't included noise in our analysis. Inclusion of noise would reduce the signal-to-noise (S/N).
- **Comparison against theory:** Computation of the IB depends on a particular model of bispectrum. In the past various scenarios such as the Standard (Eulerian) perturbation theory (SPT; at two and three loops) (see Figure-1), halo models, separate Universe models and effective field theories (see Figure-2) were used. We have presented a number of approaches and shown that as far as the theoretical predictions are considered there is a huge variation in the underlying 3D bispectrum depending on the underlying model, e.g. EFT results points to a lower values of the IB for high- $k$  compared to SPT whereas, other methods predict higher than SPT values. Ideally, to be consistent the parameters defining a specific implementation of EFT should be extracted from the N-body simulations from which the convergence maps are obtained through ray-tracing simulations. However, this is outside the scope of our current study. Indeed, one can also use an accurate *fitting functions* for the bispectrum to derive the squeezed limit and the resulting IB [39]. Most such fitting functions include the Hierarchal Ansatz (introduced before) as a high  $k$  limiting situation. We have tested the predictions for hierarchal ansatz coupled to HEPT for the high  $\ell$  regime and find reasonable agreement. This is encouraging as it proves that a full non-linear calculation may provide accurate prediction for the entire range of  $\ell$  values.

The presence of the bias due to finite volume (area) correction makes a direct comparison difficult. Thus, in this work we have restricted our comparison against the SPT. Though, we have provided detailed derivations of other methods of theoretical modeling. For SPT, we have assumed a locally power law power spectrum which simplifies theoretical analysis. We have used three spectral index  $n = -1.0, -1.5$  and  $-2.0$  to the variation in theoretical prediction.

## 7 Conclusions and Future Prospects

We have used the IB to probe the gravity induced non-Gaussianity from simulated weak lensing maps. The results derived are valid for generic projected surveys. Using the small angle approximation we show how an estimator for the IB can bypass many of the complexities associated with the estimation of the entire bispectrum. By further focusing on the squeezed limit the IB, we can avoid many of the issues associated with estimation of bispectrum,

and can compute the IB using ordinary power spectrum estimation techniques. Indeed, this comes at a price as information is only available in the squeezed limit. We discuss below some key-aspects of our study and point to future directions:

1. **Tomography and Bayesian generalization:** Extending flat-sky results we also develop a full-sky estimator for the IB. These estimators take advantage of the existing Pseudo- $\mathcal{C}_\ell$  estimators developed for power spectrum analysis. A tomographic generalization can be implemented by correlating convergence maps from one bin against power spectrum from the same or different bins. We also point out that the estimators based on pseudo- $\mathcal{C}_\ell$  can also be extended to a Bayesian version by using a Bayesian power spectrum estimator (see e.g. [54, 55]).
2. **Theoretical estimates:** We have developed analytical estimates of IB using various approximations to gravitational clustering including variants of halo-models, tree-level perturbation theory as well as using EFT.
3. **Test against *Euclid* Flagship simulations:** We have used the Euclid Flagship simulations to test our result using the convergence or  $\kappa$  maps. We have studied the impact of resolution, patch-size and level of non-Gaussianity as a function of redshift  $z$ . We compare the results against theoretical predictions and find reasonable agreement. We have presented a rather simplistic model for error analysis. More realistic analysis of error covariance will be presented elsewhere.
4. **Generalization of IB to shear  $\gamma$  and other spin-2 objects:** Our results can be easily generalized to shear  $\gamma$  maps and directly used to analyse the maps from ongoing and planned weak lensing surveys. In this case one would replace the pseudo- $\mathcal{C}_\ell$  estimator for spin-0 scalar field with a spin-2 estimator for “Electric” E and “Magnetic” B power spectra. A correlation of these spectra with the E and B maps will provide a squeezed estimator for the pure EEE, and BBB bispectrum or mixed EEB and EBB type bispectrum. The first two estimators correspond to the correlators  $\langle \bar{E}C_\ell^{EE} \rangle$  and  $\langle \bar{B}C_\ell^{BB} \rangle$ . The squeezed limits of mixed bispectra are constructed in a similar manner i.e.  $\langle \bar{B}C_\ell^{EE} \rangle$  and  $\langle \bar{E}C_\ell^{BB} \rangle$ .
5. **Position-dependent correlation functions:** Correlations functions carry the same information as their Fourier counterparts. In case of masks with complex topology it may be useful to compute the *position-dependent* two-point correlation function. This will probe the squeezed limit of the three-point correlation function (Munshi et al. (2019) in preparation). Such an approach can be specially useful for surveys with small sky coverage.
6. **Relation to other estimators:** The other estimators of bispectrum include the skew-spectrum which can be useful as it too collapses the information content of the bispectrum from three wave numbers in the harmonic domain to just one. The skew-spectrum is an important estimator for the bispectrum though it mixes various shapes and is not just sensitive to the squeezed limit. The squeezed limit has interesting relationship to various consistency relations discussed in the recent past [77–79].
7. **Numerical implementation:** Exploration of the entire configuration dependence of the bispectrum requires elaborate computation. Both IB as well as the skew-spectrum

can also be seen as a method of data compression beyond what can be achieved by one-point estimators such as the skewness probes specific aspects of the bispectrum.

8. **Beyond bispectrum to higher-order:** The idea of the skew-spectrum has already been extended to higher-order power spectrum which leads to two different kurtosis spectra. A similar extensions is possible in case of IB to higher-order which will probe the collapsed and squeezed configurations of the trispectrum. The collapsed spectra will correspond to the covariance of the IB and the squeezed limit of the tripsectrum will represent the position dependent bispectrum. These estimators can be useful in situations where the bispectrum vanishes identically and the trispectrum remains the dominant contribution to non-Gaussianity. In surveys with high S/N it would be possible to extend such methods beyond the kurtosis spectra to fifth-order or even higher. Corresponding correlation functions in real space will also be equally effective non-Gaussianity statistics for weak lensing surveys. However, the effect of finite area covered by the survey will increasingly play a dominant role and techniques must be developed to correct such effect.
9. **External data sets and *mixed* IB:** The estimator for IB can be generalized to investigate mixed bispectrum of two different data sets, e.g. cross-correlating the power spectrum estimates from CMB secondaries, such as the all-sky  $y$ -parameter power spectrum estimates from e.g. Planck  $C_\ell^{yy}$ , and cross-correlating against  $\bar{\kappa}$  estimated from the same patch of sky  $\langle \bar{\kappa} C_\ell^{yy} \rangle$ , will provide information about  $yy\kappa$  bispectrum in squeezed configurations. An estimator for  $\kappa\kappa y$  bispectrum too can be constructed in an analogous manner  $\langle \bar{\kappa} C_\ell^{yy} \rangle$ .

Such extensions will be presented in future work.

## References

- [1] Planck 2018 results. VI. Cosmological parameters, Planck Collaboration, [[arxiv/1807.06209](https://arxiv.org/abs/1807.06209)]
- [2] Beyond the Cosmological Standard Model, A. Joyce, B. Jain, J. Khoury, M. Trodden, 2015, Phys. Rep., 568, 1 [[astro-ph/1407.0059](https://arxiv.org/abs/1407.0059)]
- [3] Modified Gravity and Cosmology, T. Clifton, P. G. Ferreira, A. Padilla, S. Skordis, 2012, Phys. Rep., 513, 1, 1 [[astro-ph/1106.2476](https://arxiv.org/abs/1106.2476)]
- [4] Massive neutrinos and cosmology, J. Lesgourgues, S. Pastor, 2006, Phys. Rep., 429, 307, [[astro-ph/1610.02956](https://arxiv.org/abs/1610.02956)]
- [5] Cosmology from Cosmic Shear with DES Science Verification Data, The Dark Energy Survey Collaboration, T. Abbott, F. B. Abdalla, S. Allam, et al., 2016, Phys. Rev. D, 94, 022001 [[arxiv/1507.0552](https://arxiv.org/abs/1507.0552)]
- [6] Gravitational Lensing Analysis of the Kilo Degree Survey, K. Kuijken, C. Heymans, H. Hildebrandt, et al., 2015, MNRAS, 454, 3500 [[astro-ph/1507.00738](https://arxiv.org/abs/1507.00738)]
- [7] *Euclid* Definition Study Report, R. Laureijs, J. Amiaux, S. Arduini, et al. 2011, ESA/SRE(2011)12.
- [8] LSST: a complementary probe of dark energy, J. A. Tyson, D. M. Wittman, J. F. Hennawi, D. N. Spergel, 2003, Nuclear Physics B Proceedings Supplements, 124, 21 [[astro-ph/0209632](https://arxiv.org/abs/astro-ph/0209632)]
- [9] National Research Council. 2010. New Worlds, New Horizons in Astronomy and Astrophysics. The National Academies Press. <https://doi.org/10.17226/12951>.

- [10] Cosmology with Weak Lensing Surveys, D. Munshi, P. Valageas, L. Van Waerbeke, A. Heavens, 2008, Phys. Rep, 462, 67 [[arXiv/0612667](#)]
- [11] SDSS-III: Massive Spectroscopic Surveys of the Distant Universe, the Milky Way Galaxy, and Extra-Solar Planetary Systems, D. J. Eisenstein, D. H. Weinberg, E. Agol, et al., 2011, AJ, 142, 72 [[astro-ph/1101.1529](#)]
- [12] The WiggleZ Dark Energy Survey: Survey Design and First Data Release, Drinkwater, M. J., R. J. Jurek, C. Blake, et al., 2010, MNRAS, 401, 14 [[astro-ph/0911.4246](#)]
- [13] Large-Scale Galaxy Bias, V. Desjacques, D. Jeong, F. Schmidt, 2018, Phys. Rep. 733, 1 [[arXiv/1611.09787](#)]
- [14] Large scale structure of the universe and cosmological perturbation theory, F. Bernardeau, S. Colombi, E. Gaztanaga, R. Scoccimarro, 2002, Phys.Rep. 367, 1 [[astro-ph/0112551](#)]
- [15] Weak lensing analysis in three dimensions, P. G. Castro, A. F. Heavens, T. D. Kitching, 2005, Phys Rev D, 72, 3516 [[astro-ph/0503479](#)]
- [16] Higher-order Statistics of Weak Lensing Shear and Flexion, D. Munshi, J. Smidt, A. Heavens, P. Coles, A. Cooray 2011, MNRAS, 411, 2241 [[astro-ph/1003.5003](#)]
- [17] Higher-order Convergence Statistics for Three-dimensional Weak Gravitational Lensing, D. Munshi, A. Heavens, P. Coles, 2011, MNRAS, 411, 2161 [[astro-ph/1002.2089](#)]
- [18] Higher Order Statistics for Three-dimensional Shear and Flexion, D. Munshi, T. Kitching, A. Heavens, P. Coles, 2011, MNRAS, 416, 629 [[astro-ph/1012.3658](#)]
- [19] On the estimation of gravity-induced non-Gaussianities from weak lensing surveys, P. Valageas, D. Munshi, A. J. Barber, 2005, MNRAS. 356, 386 [[astro-ph/0402227](#)]
- [20] Weak lensing shear and aperture-mass from linear to non-linear scales, D. Munshi, P. Valageas, A. J. Barber, 2004, MNRAS 350, 77 [[astro-ph/0309698](#)]
- [21] From linear to non-linear scales: analytical and numerical predictions for the weak lensing convergence, A. J. Barber, D. Munshi, P. Valageas, 2004, MNRAS, 347, 667 [[astro-ph/0304451](#)]
- [22] Testing Inflation with Large Scale Structure: Connecting Hopes with Reality, M. Alvarez et al., [[arXiv/1412.4671](#)]
- [23] Statistics of Weak Lensing at Small Angular Scales: Analytical Predictions for Lower Order Moments, D. Munshi, B. Jain, 2001, MNRAS, 322, 107 [[astro-ph/9912330](#)]
- [24] Probing The Gravity Induced Bias with Weak Lensing: Test of Analytical results Against Simulations, D. Munshi, 2000, MNRAS, 318, 145 [[astro-ph/0001240](#)]
- [25] A New Approach to Probing Primordial Non-Gaussianity, D. Munshi, A. Heavens, 2010, MNRAS, 401, 2406 [[arXiv/0904.4478](#)]
- [26] New Optimised Estimators for the Primordial Trispectrum, D. Munshi, A. Heavens, A. Cooray, J. Smidt, P. Coles, P. Serra, 2011, MNRAS, 412, 1993 [[arXiv/0910.3693](#)]
- [27] The Statistics of Weak Lensing at Small Angular Scales: Probability Distribution Function, D. Munshi, B. Jain, 2000, MNRAS, 318, 109 [[astro-ph/9911502](#)]
- [28] Analytical Predictions for Statistics of Cosmic Shear: Tests Against Simulations, P. Valageas, A. J. Barber, D. Munshi 2004, MNRAS, 347, 654 [[astro-ph/0303472](#)]
- [29] Position-dependent correlation function from the SDSS-III Baryon Oscillation Spectroscopic Survey Data Release 10 CMASS Sample, C.-T. Chiang, C. Wagner, A. G. Sanchez, F. Schmidt, E. Komatsu 2015, JCAP, 09, 028 [[astro-ph/1504.03322](#)]
- [30] The Lyman- power spectrum - CMB lensing convergence cross-correlation, C.-T. Chiang, A. Slosar, 2018, JCAP, 01, 012 [[arXiv/1708.07512](#)]

- [31] Response approach to the squeezed-limit bispectrum: application to the correlation of quasar and Lyman- forest power spectrum, C.-T. Chiang, A. M. Cieplak, F. Schmidt, A. Slosar, 2017, JCAP, 06, 022 [[arXiv/1701.03375](#)]
- [32] Position-dependent power spectrum: a new observable in the large-scale structure, C.-T. Chiang, [[arXiv/1508.03256](#)]
- [33] The Integrated Bispectrum and Beyond, D. Munshi, P. Coles, 2017, JCAP, 02, 010 [[arXiv/1608.04345](#)]
- [34] Position-dependent power spectrum of the large-scale structure: a novel method to measure the squeezed-limit bispectrum C.-T. Chiang, C. Wagner, F. Schmidt, E. Komatsu 2014, JCAP, 05, 048 [[arXiv/1403.3411](#)]
- [35] Hyperextended Cosmological Perturbation Theory: Predicting Non-linear Clustering Amplitudes R. Scoccimarro, J. A. Frieman 1999, ApJ. 520, 35 [[astro-ph/9811184](#)]
- [36] The Integrated Bispectrum in Modified Gravity Theories, D. Munshi, 2017, JCAP, 01, 049 [[arXiv/1610.02956](#)]
- [37] The angular correlation hierarchy in the quasilinear regime, F. Bernardeau, 1995, A&A, 301, 309 [[arXiv/9502089](#)]
- [38] Consistency Relations in Effective Field Theory, D. Munshi, D. Regan, 2017, JCAP, 06, 042 [[arXiv/1705.07866](#)]
- [39] An improved fitting formula for the dark matter bispectrum, H. Gil-Marn, C. Wagner, F. Fragkoudi, R. Jimenez, L. Verde 2012, JCAP, 02, 047 [[arXiv/1111.4477](#)]
- [40] Separating the Universe into the Real and Fake, W. Hu, C.-T. Chiang, Y. Li, M. LoVerde, 2016, Phs. Rev. D, 94, 023002 [[arXiv/1605.01412](#)]
- [41] Scale-dependent bias and bispectrum in neutrino separate universe simulations, C.-T. Chiang, W. Hu, Y. Li, M. LoVerde, 2018, Phys. Rev. D, 97, 123526 [[arXiv/1710.01310](#)]
- [42] NonGaussianity from Inflation: Theory and Observations, N. Bartolo, E. Komatsu, S. Matarrese, A. Riotto, 2004, Phys.Rep., 402, 103 [[arXiv/0406398](#)]
- [43] The halo squeezed-limit bispectrum with primordial non-Gaussianity: a power spectrum response approach, C.-T. Chiang, 2017, Phys. Rev. D, 95, 123517 [[arXiv/1701.03374](#)]
- [44] Non-Linear Approximations to Gravitational Instability: A Comparison in the Quasi-Linear Regime, D. Munshi, V. Sahni, A. A. Starobinsky 1994, ApJ., 436, 517 [[arXiv/9402065](#)]
- [45] Planck 2015 results. XVII. Constraints on primordial non-Gaussianity, Planck Collaboration, 2016, A&A, 594, 17 [[arXiv/1502.01592](#)]
- [46] Planck 2015 results. XIV. Dark energy and modified gravity, Planck Collaboration, 2016, A&A, 594, 14 [[arXiv/1502.01590](#)]
- [47] Report of the Dark Energy Task Force A. Albrecht et al. [[astro-ph/0609591](#)]
- [48] The bispectrum of cosmic string temperature fluctuations including recombination effects, D. Regan, M. Hindmarsh, 2015, JCAP, 10, 030 [[arXiv/1508.02231](#)]
- [49] A Consistency Relation for the Observed Galaxy Bispectrum and the Local non-Gaussianity from Relativistic Corrections, A. Kehagias, A. Moradinezhad Dizgah, J. Norea, H. Perrier, A. Riotto, 2015, JCAP, 08, 018 [[arXiv/1503.04467](#)]
- [50] Weak lensing of the CMB: A harmonic approach, W. Hu, 2000, Phys.Rev. D, 62, 043007 [[arXiv/0001303](#)]
- [51] MASTER of the CMB Anisotropy Power Spectrum: A Fast Method for Statistical Analysis of Large and Complex CMB Data Sets, E. Hivon, K. M. Gorski, C. B. Netterfield, B. P. Crill, S. Prunet, F. Hansen, 2002, ApJ, 567, 2 [[arXiv/0105302](#)]



- [52] Flat-Sky Pseudo-Cls Analysis for Weak Gravitational Lensing, M. Asgari, A. Taylor, B. Joachimi, T. D. Kitching [[arXiv/1612.04664](#)]
- [53] Shear Power Spectrum Reconstruction using Pseudo-Spectrum Method, C. Hikage, M. Takada, T. Hamana, D. Spergel, MNRAS, 412, 65, 2011 [[arXiv/1004.3542](#)]
- [54] Fast optimal CMB power spectrum estimation with Hamiltonian sampling, J. F. Taylor, M. A. J. Ashdown, M. P. Hobson, 2008, MNRAS, 389, 1284 [[arXiv/0708.2989](#)]
- [55] Methods for Bayesian power spectrum inference with galaxy surveys, J. Jasche, B. D. Wandelt, 2013, ApJ, 779, 15 [[arXiv/1306.1821](#)]
- [56] Halo Models of Large Scale Structure, A. Cooray, R. Sheth, 2002, Phys.Rep., 372, 1 [[arXiv/0206508](#)]
- [57] Cosmological Non-Linearities as an Effective Fluid, D. Baumann, A. Nicolis, L. Senatore, M. Zaldarriaga, 2012, JCAP 1207, 051 [[arXiv/1004.2488](#)]
- [58] The Effective Field Theory of Cosmological Large Scale Structures, J. J. M. Carrasco, M. P. Hertzberg, L. Senatore, 2012, JHEP 09, 082 [[arXiv/1206.2926](#)]
- [59] The Bispectrum in the Effective Field Theory of Large Scale Structure, T. Baldauf, L. Mercolli, M. Mirbabayi, E. Pajer 2015, JCAP, 05, 007 [[arXiv/1406.4135](#)]
- [60] Super-Sample Signal, Y. Li, W. Hu, M. Takada, Phys. Rev. D 2014, 90, 103530 [[arXiv/1408.1081](#)]
- [61] Linear response to long wavelength fluctuations using curvature simulations, T. Baldauf, U. Seljak, L. Senatore, M. Zaldarriaga, 2016, JCAP, 09, 007 [[arXiv/1511.01465](#)]
- [62] The Shift of the Baryon Acoustic Oscillation Scale: A Simple Physical Picture, B.D. Sherwin, M. Zaldarriaga, 2012, Phys. Rev. D 85, 103523 [[arXiv/1202.3998](#)]
- [63] On Separate Universes, L. Dai, E. Pajer, F. Schmidt, 2015, JCAP, 10, 059 [[arXiv/1504.00351](#)]
- [64] The Coyote Universe Extended: Precision Emulation of the Matter Power Spectrum, K. Heitmann, E. Lawrence, J. Kwan, S. Habib, D. Higdon 2014, ApJ, 780, 111 [[arXiv/1304.7849](#)]
- [65] A Fitting Formula for the Non-Linear Evolution of the Bispectrum, R. Scoccimarro, H.M.P. Couchman, 2001, MNRAS, 325, 1312 [[arXiv/0009427](#)]
- [66] PKDGRAV3: beyond trillion particle cosmological simulations for the next era of galaxy surveys D. Potter, J. Stadel, R. Teyssier, 2017, ComAC, 4, 1
- [67] The onion universe: all sky lightcone simulations in spherical shells, P. Fosalba, E. Gaztaaga, F. J. Castander, J. Francisco, M. Manera, 2008, MNRAS, 391, 435 [[arXiv/0711.1540](#)]
- [68] The MICE Grand Challenge light-cone simulation - III. Galaxy lensing mocks from all-sky lensing maps, P. Fosalba, E. Gaztaaga, F. J. Castander, M. Crocce, 2015, MNRAS, 447, 1319 [[arXiv/1312.2947](#)]
- [69] Castander et al. (2019), in prep.
- [70] An algorithm to build mock galaxy catalogues using MICE simulations Carretero, J.; Castander, F. J.; Gaztaaga, E.; Crocce, M.; Fosalba, P. 2015, MNRAS, 447, 646
- [71] Effects of Sampling on Statistics of Large Scale Structure, S. Colombi, I. Szapudi, A.S. Szalay, 1998, MNRAS, 296, 253 [[arXiv/9711087](#)]
- [72] Cosmic Error and the Statistics of Large Scale Structure, I. Szapudi, S. Colombi, 1996, ApJ, 470, 131 [[arXiv/9711087](#)]
- [73] Scaling in Gravitational Clustering, 2D and 3D Dynamics, D. Munshi, F. Bernardeau, A. L. Melott, R. Schaeffer, 1999, MNRAS, 303, 433 [[arXiv/9510030](#)]
- [74] The Limits of Cosmic Shear, T. D. Kitching, J. Alsing, A. F. Heavens, R. Jimenez, J. D.

- McEwen, L. Verde, 2017, MNRAS, 469, 2737 [[arXiv/1611.04954](#)]
- [75] The effect of Limber and flat-sky approximations on galaxy weak lensing, P. Lemos, A. Challinor, G. Efstathiou, 2017, JCAP, 05, 014 [[arXiv/1704.01054](#)]
- [76] Precision calculations of the cosmic shear power spectrum projection, M. Kilbinger, 2017, MNRAS, 472, 2126 [[arXiv/1702.05301](#)]
- [77] Consequences of Symmetries and Consistency Relations in the Large-Scale Structure of the Universe for Non-local bias and Modified Gravity, A. Kehagias, J. Norena, H. Perrier, A. Riotto, 2014, Nuclear Physics B, 883, 83, [[arXiv/1311.0786](#)]
- [78] Symmetries and consistency relations in the large scale structure of the universe, A. Kehagias, A. Riotto, 2013, Nuclear Physics B, 873, 514, [[arXiv/1004.3542](#)]
- [79] Ward identities and consistency relations for the large scale structure with multiple species M. Peloso, M. Pietroni, 2014, JCAP, 4, 011 [[arXiv/1004.3542](#)]
- [80] Statistical properties of the convergence due to weak gravitational lensing by non-linear structures, P. Valageas, 2000, A & A, 356, 771 [[astro-ph/9911336](#)]
- [81] Probing the Gravity Induced Bias with Weak Lensing: Test of Analytical results Against Simulations, D. Munshi, 2000, MNRAS, 318, 145 [[astro-ph/00001240](#)]
- [82] Lognormal Property of Weak Lensing Fields, A. Taruya, M. Takada, T. Hamana, I. Kayo, T. Futamase, 2002, ApJ, 571, 638 [[astro-ph/0202090](#)]

## Acknowledgment

DM is supported by a grant from the Leverhume Trust. TDK is supported by Royal Society University Research Fellowship. It's a pleasure for DM to acknowledge many helpful discussions with Andrea Petri, Peter Taylor, Alexander Eggemeier and Chi-Ting Chiang for useful comments. It is our pleasure also to acknowledge constructive comments from P. Schneider and V. F. Cardone.

## A Approximate Line-of-Sight Integration

In this appendix we discuss how the line-of-sight integrals can be approximated that leads to separation of projection effects and the dynamical effect. It was shown in [23, 80] that the scaled convergence field  $\kappa/|\kappa_{\min}|$  (see Eq.(3.6b) for a definition) statistically behaves exactly like the underlying density contrast  $\delta$ : Thus  $\kappa_{\min}$  is the minimum value  $\kappa$  can reach when  $\delta = -1$  (representing the void regions) along the entire line-of-sight in Eq.(2.8). Notice  $\kappa_{\min}$  doesn't depend on smoothing and it is a global quantity. This was checked in great detail against simulations as was found to be extremely successful in describing cumulants, cumulant correlators [81] as well as the Minkowski Functionals [82].

In the context of one-point probability density function (PDF), the normalized cumulant  $S_3$  of the underlying density contrast  $\delta$  defined as  $S_3 := \langle \delta^3 \rangle_c / \langle \delta^2 \rangle_c^2$  is related to that of  $\kappa$  defined as  $S_3^\kappa := \langle \kappa^3 \rangle_c / \langle \kappa^2 \rangle_c^2$ . The exact relation can be derived using the line-of-sight integration. However, using the  $\delta \rightarrow \kappa/|\kappa_{\min}|$  mapping an approximate but very accurate and simple result can be obtained  $S_3^\kappa = S_3/|\kappa_{\min}|$ . Similarly, for the two-point probability density function, the third-order statistics  $C_{21} := \langle \delta_1^2 \delta_2 \rangle_c / \langle \delta_1 \delta_2 \rangle_c$  (in our notation  $\delta_1 := \delta(\mathbf{x}_1)$ ) for  $\kappa$  and  $\delta$ , denoted as  $C_{21}$  and  $C_{21}^\kappa$ , can be related in an analogous manner i.e.  $C_{21}^\kappa = C_{21}/|\kappa_{\min}|$ . This is consistent with our derivation for the IB which is also a third-order statistics. We have

used the mapping  $\delta \rightarrow \kappa/|\kappa_{\min}|$  and resulting  $R_2 \rightarrow 1/|\kappa_{\min}|$  in simplifying the theoretical predictions in §3. To see how this approximation can simplify the analytical calculation in §3 we note that if we approximate the numerator and the denominator of Eq.(2.18b) defining  $R_2$  as  $\int_0^{r_s} dr f(r) \approx r_s f(r_c)/2$  ( $r_c$  is the value of  $r$  for which the integrand  $f(r)$  reaches its maximum value) we get  $R_2 \approx 1/[2r_c w(r_c)]$  which is same as  $R_2 \approx 1/|\kappa_{\min}|$ . So Eq.(2.19) can be approximated as:

$$\mathcal{B}'(l) \approx \frac{1}{|\kappa_{\min}|} \left[ \frac{24}{7} - \frac{1}{2} \frac{d \ln l^2 P_{3D}(l)}{d \ln l} \right]. \quad (\text{A.1})$$

The numerical factor within the parenthesis can be derived using 2D spherical dynamics [37]. Similar approximation can also be used to simplify Eq.(2.23) using the 2D spherical dynamics in the context of ZA.